nature cell biology

ARTICLES

https://doi.org/10.1038/s41556-021-00699-6

Check for updates

# Mechanical compartmentalization of the intestinal organoid enables crypt folding and collective cell migration

Carlos Pérez-González[1,2,3,11], Gerardo Ceada[1,2,11], Francesco Greco[4], Marija Matejčić[1], Manuel Gómez-González[1], Natalia Castro[1], Anghara Menendez[1], Sohan Kale[4,5], Denis Krndija[3], Andrew G. Clark[3], Venkata Ram Gannavarapu[3], Adrián Álvarez-Varela[6,7], Pere Roca-Cusachs[1,2], Eduard Batlle[6,7,8], Danijela Matic Vignjevic[3] ✉, Marino Arroyo[1,4,9] ✉ and Xavier Trepat[1,2,8,10] ✉

**Intestinal organoids capture essential features of the intestinal epithelium such as crypt folding, cellular compartmentalization and collective movements. Each of these processes and their coordination require patterned forces that are at present unknown. Here we map three-dimensional cellular forces in mouse intestinal organoids grown on soft hydrogels. We show that these organoids exhibit a non-monotonic stress distribution that defines mechanical and functional compartments. The stem cell compartment pushes the extracellular matrix and folds through apical constriction, whereas the transit amplifying zone pulls the extracellular matrix and elongates through basal constriction. The size of the stem cell compartment depends on the extracellular-matrix stiffness and endogenous cellular forces. Computational modelling reveals that crypt shape and force distribution rely on cell surface tensions following cortical actomyosin density. Finally, cells are pulled out of the crypt along a gradient of increasing tension. Our study unveils how patterned forces enable compartmentalization, folding and collective migration in the intestinal epithelium.**

Most epithelial tissues that line the internal and external surfaces of the animal body perform their diverse physiological functions in a continuous state of self-renewal[1]. In the intestinal epithelium, rapid self-renewal is enabled by stem cells that reside at the bottom of highly curved invaginations called crypts, where they coexist with secretory Paneth cells[2]. To maintain homeostasis, stem cells constantly divide, giving rise to new cells that proliferate further at the transit amplifying zone, differentiate and migrate to the tip of finger-like protrusions called villi, where they are extruded into the intestinal lumen[3,4].

The intestinal epithelium self-renews while retaining a folded shape. Villus folding is driven by compressive stresses generated by the mesenchyme or smooth muscle[5–7]. By contrast, how the crypt folds during morphogenesis and how folding is maintained during homeostasis is not well understood. Candidate folding mechanisms include buckling as a consequence of increased mitotic pressure[8–11], differentials in actomyosin forces between epithelial compartments[12] or planar cellular flows[13]. In addition, crypt folding could arise from bending by apical constriction[14,15], basal expansion[16] or trans-epithelial differences in osmotic pressure[17,18]. Importantly, the cellular forces that fold the epithelium must also enable other mechanical functions such as collective movement from the crypt to the villus[4]. How forces are distributed in the intestinal epithelium to drive its diverse mechanical functions is unknown. Using the mouse intestinal organoid as a model system[19–24], here we provide high-resolution dynamic maps of cell–extracellular matrix (ECM) and cell–cell forces exerted by the intestinal epithelium. Our experiments and computational model reveal that the intestinal epithelium is organized in mechanical compartments, in which patterned forces drive folding by apical constriction while enabling cell migration along tensile gradients.

## Results

**Organoid monolayers display mechanical compartments.** We isolated intestinal crypts from mice and seeded them on soft (5 kPa) polyacrylamide (PAA) gels coated with collagen I and laminin 1. The crypts adhered readily on the flat substrates and spread in a process akin to active tissue wetting (Fig. 1a and Supplementary Video 1)[25]. A few days after crypt spreading, the substrate was covered by a continuous monolayer that showed compartmentalization of the main cell types of the intestinal epithelium[26–30] (Fig. 1b and Extended Data Fig. 1). Stem (labelled with Lgr5 and Olfm4) and Paneth (labelled with lysozyme) cells were intermingled in a roughly circular compartment devoid of any other cell type. This stem cell compartment was surrounded by a ring of highly proliferative cells (positive for Ki67) elongated in the direction parallel to the crypt contour. Cells outside of this ring expressed the differentiation marker cytokeratin 20 and increased their spreading

[1]Institute for Bioengineering of Catalonia (IBEC), The Barcelona Institute for Science and Technology (BIST), Barcelona, Spain. [2]Facultat de Medicina, Universitat de Barcelona, Barcelona, Spain. [3]Institut Curie, PSL Research University, CNRS UMR, Paris, France. [4]LaCàN, Universitat Politècnica de Catalunya–BarcelonaTech, Barcelona, Spain. [5]Mechanical Engineering Department, Virginia Tech, Blacksburg, VA, USA. [6]Institute for Research in Biomedicine (IRB Barcelona), Barcelona Institute of Science and Technology (BIST), Barcelona, Spain. [7]Centro de Investigación Biomédica en Red de Cáncer (CIBERONC), Barcelona, Spain. [8]Institució Catalana de Recerca i Estudis Avançats (ICREA), Barcelona, Spain. [9]Centre Internacional de Mètodes Numèrics en Enginyeria (CIMNE), Barcelona, Spain. [10]Centro de Investigación Biomédica en Red en Bioingeniería, Biomateriales y Nanomedicina (CIBER-BBN), Barcelona, Spain. [11]These authors contributed equally: Carlos Pérez-González, Gerardo Ceada. ✉e-mail: danijela.vignjevic@curie.fr; marino.arroyo@upc.edu; xtrepat@ibecbarcelona.eu

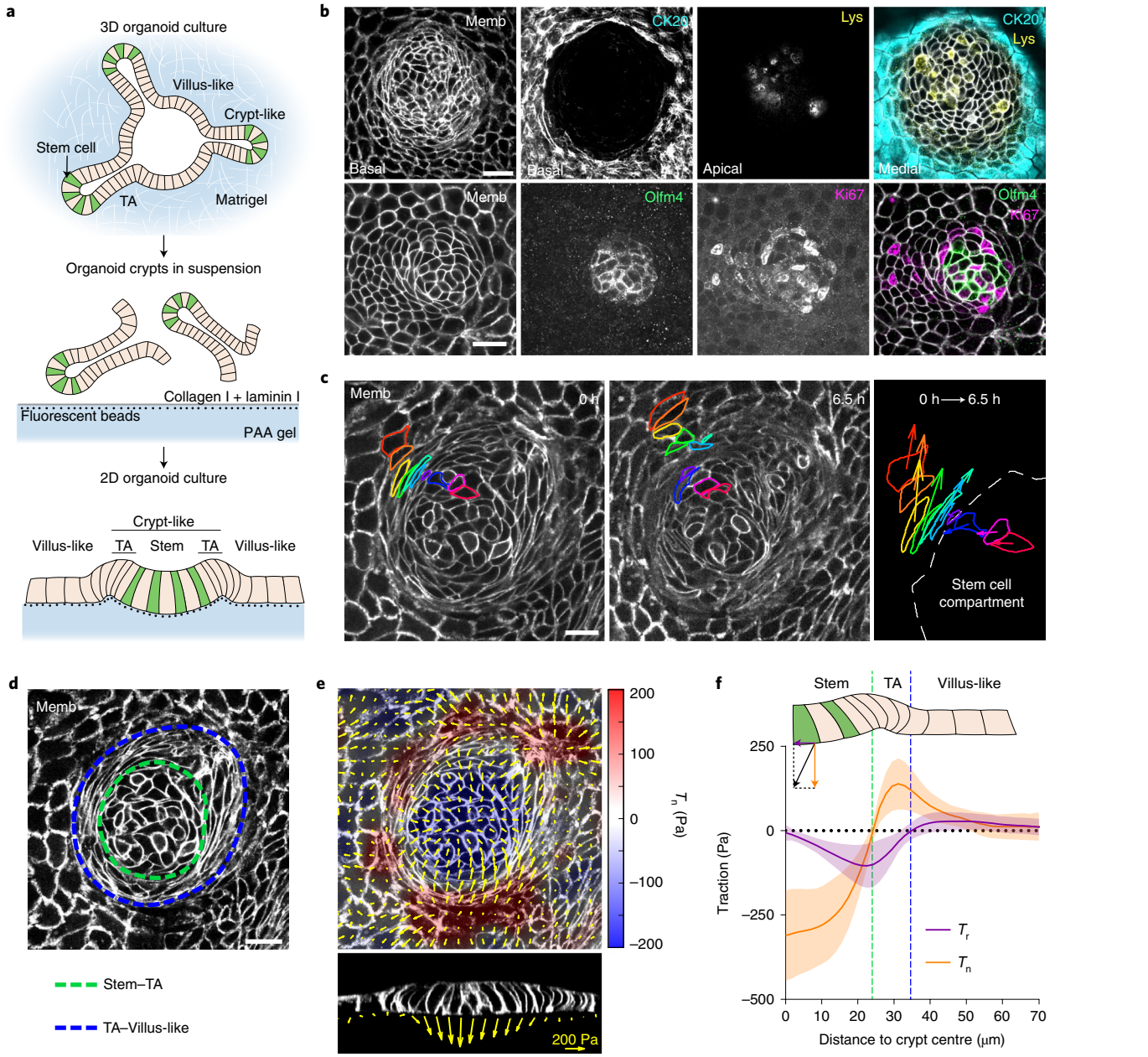


**Fig. 1 | Tractions exerted by intestinal organoids define mechanical compartments. a**, Preparation of mouse intestinal organoids on 2D soft substrates. **b**, Organoids expressing membrane-targeted tdTomato (Memb, basal plane) stained for cytokeratin 20 (CK20, basal plane), lysozyme (Lys, apical plane), Olfm4 (basal plane) and Ki67 (basal plane). Images are representative of three independent experiments. **c**, Displacement of representative cells over 6.5 h (left and middle). Each colour labels one cell. Note that one cell divided (green). Displacement vector of each cell (right). See also Supplementary Video 3. Images are representative of three independent experiments. **d**, Illustration of the boundaries between the stem cell compartment and transit amplifying zone (green), and the transit amplifying zone and villus-like domain (blue). **b**–**d**, Scale bars, 20 μm. **e**, Three-dimensional traction maps overlaid on a top view of an organoid (top). The yellow vectors represent components tangential to the substrate and the colour map represents the component normal to the substrate. Lateral view along the crypt horizontal midline (bottom). The yellow vectors represent tractions. Scale vector, 200 Pa. Representative of seven independent experiments. **f**, Circumferentially averaged normal and radial tractions as a function of the distance to the crypt centre. The blue and green dashed lines indicate the radii where $T_n$ and $T_r$, respectively, are zero, which closely correspond to the boundaries between the functional compartments illustrated in **d**. The $T_r$ value at the villus is significantly different from zero (one-sample Wilcoxon test, $P < 0.0001$). Data are represented as the mean ± s.d. of $n = 37$ crypts from seven independent experiments. TA, transit amplifying zone; 5 kPa PAA substrates.

area. These results show that although curvature may influence self-renewal of the intestinal epithelium[31], it is not required for its compartmentalization.

We next investigated whether the cells in each compartment retained their in vivo homeostatic functions. Time-lapse imaging showed that the stem cells divided frequently and that the daughter cells entered the highly proliferative zone, where they divided further (Fig. 1c and Supplementary Videos 2,3). On leaving this zone, the cells continued to move into the differentiated zone, where they were extruded (Fig. 1c, Extended Data Fig. 1c and

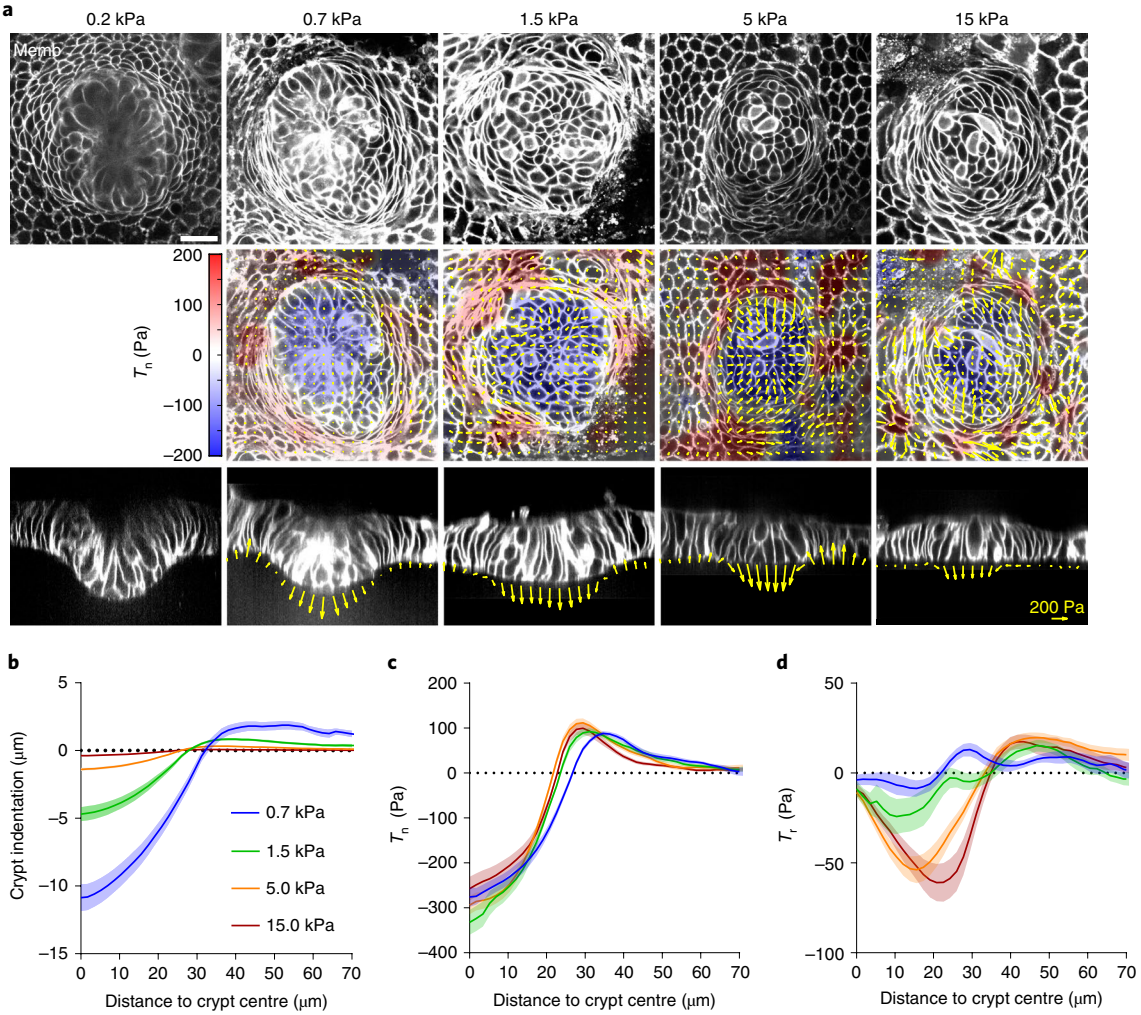


**Fig. 2 | A stiffness-independent normal traction folds the crypt. a**, Single confocal plane of representative crypts on substrates of increasing stiffness (top). Three-dimensional traction maps (centre). The yellow vectors represent components tangential to the substrate and the colour map represents the component normal to the substrate. Lateral view along the crypt midline (bottom). The yellow vectors represent tractions. Scale bar, 20 μm. Representative images of $n = 14$ (0.2 kPa), 23 (0.7 kPa), 23 (1.5 kPa), 37 (5 kPa) and 30 (15 kPa) crypts from 2, 3, 3, 7 and 4 independent experiments, respectively. **b**–**d**, Crypt indentation (**b**), normal traction (**c**) and radial traction (**d**) as a function of the distance to the crypt centre for substrates of different stiffness. Data are represented as the mean ± s.e.m. of $n = 23$ (0.7 kPa), 23 (1.5 kPa), 37 (5 kPa) and 30 (15 kPa) for **b**, and $n = 14$ (0.7 kPa), 12 (1.5 kPa), 36 (5 kPa) and 30 (15 kPa) crypts for **c**,**d** from 3, 3, 7 and 4 independent experiments, respectively.

Supplementary Videos 4,5). Following division at the boundary of the stem cell compartment, some daughter cells moved towards the centre of the crypt, consistent with the idea that border cells can gain short-term self-renewal potential by changing their radial position within the niche[3] (Extended Data Fig. 1d and Supplementary Video 6). Given the analogy between an organoid monolayer and the intestinal epithelium in vivo, we adopted the following nomenclature: the region containing only stem and Paneth cells is called the stem cell compartment, the region containing highly proliferative elongated cells is called the transit amplifying zone and the region containing differentiated cells is called the villus-like domain (Fig. 1b,d).

We used traction microscopy to map the three-dimensional (3D) traction forces exerted by the epithelial monolayer on its underlying substrate[18,32]. Traction maps revealed systematic mechanical patterns that were radially symmetrical about the crypt centre (Fig. 1d,e). We decomposed these traction patterns into a normal ($T_n$, perpendicular to the substrate) and a radial ($T_r$, parallel to the substrate) component. At the stem cell compartment, the normal tractions were negative, indicating that the stem and Paneth cells pushed the substrate downwards (Fig. 1e,f). The magnitude of the normal tractions was highest at the crypt centre, decreased radially away from it and vanished at the margin of the stem cell compartment. The normal tractions became positive at the transit amplifying zone, indicating that the cells in this region pulled the substrate upwards. After peaking at the transit amplifying zone, the normal tractions decreased in the villus-like domain, except in a few areas where the monolayer had delaminated to form pressurized domes (Extended Data Fig. 1e)[18]. The radial component of the traction field was negligible at the centre of the stem cell compartment and became progressively negative (that is, pointing inwards) towards its border, where it peaked near the transit amplifying zone. At the outer border of this zone, the radial tractions vanished and became slightly but significantly positive (that is, pointing outwards) in the villus-like domain (Fig. 1e,f). These measurements reveal that the intestinal epithelium generates non-monotonic traction fields on the substrate, defining distinct mechanical compartments that colocalize with functional compartments; the stem cell compartment

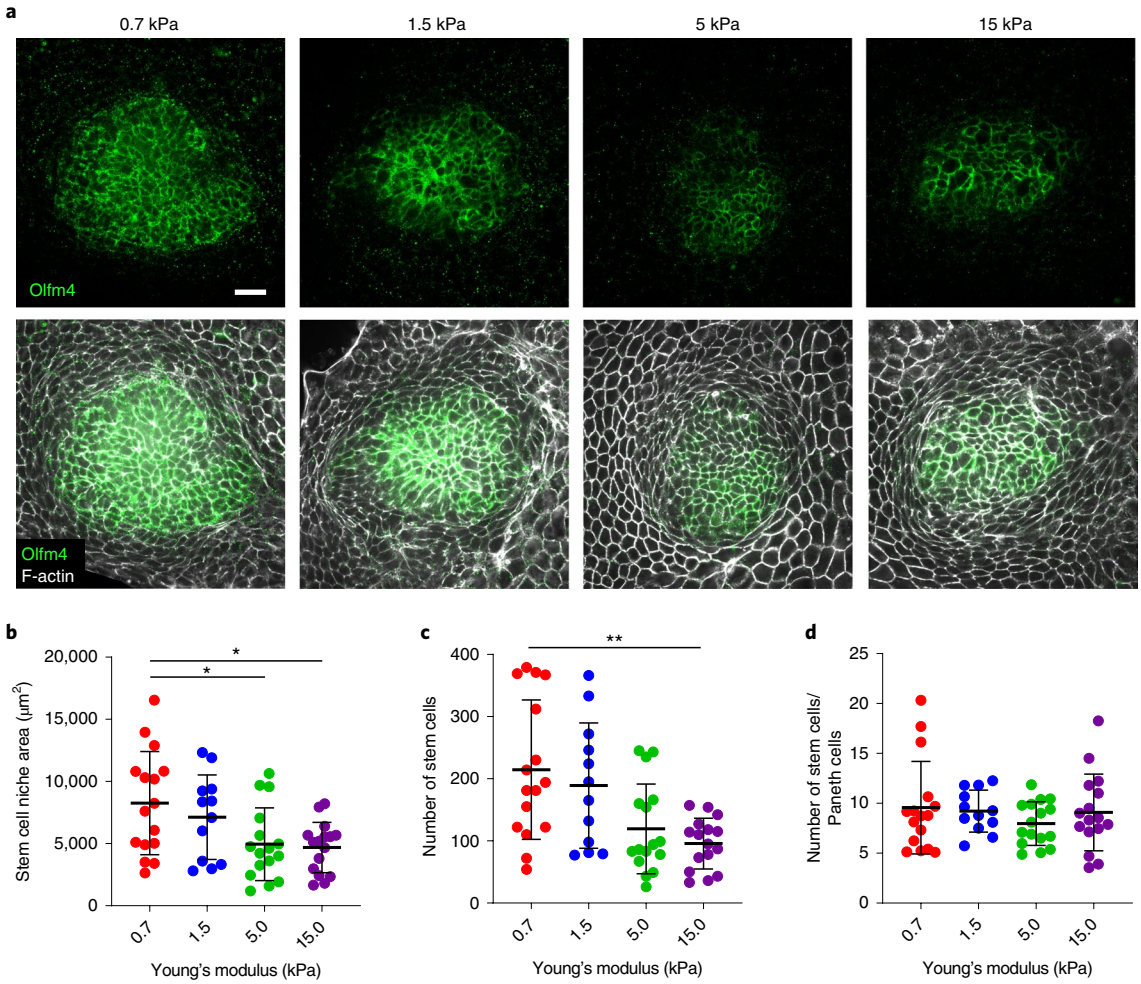


**Fig. 3 | The size of the stem cell compartment decreases with substrate rigidity. a**, Olfm4 and F-actin (phalloidin) immunostaining on substrates of increasing stiffness. Due to pronounced crypt folding, for visualization purposes, the image for 0.7 kPa is a projection along the crypt medial plane. Representative images of three independent experiments. Scale bar, 20 μm. **b**–**d**, The area of the stem cell compartment (**b**), number of stem cells (**c**) and ratio between the number of stem and Paneth cells (**d**) for substrates of increasing stiffness; $n = 16$ (0.7, 5 and 15 kPa) and 12 (1.5 kPa) crypts from three independent experiments. Statistical significance was determined using a one-way analysis of variance, followed by a Tukey's multiple-comparison test (**b**), and a Kruskal–Wallis test, followed by a Dunn's multiple-comparison test (**c**,**d**). Only statistically different pairwise comparisons are indicated. **b**, $P = 0.0305$ (0.7 versus 5 kPa) and 0.0157 (0.7 versus 15 kPa). **c**, $P = 0.0071$ (0.7 versus 15 kPa). $^*P < 0.05$ and $^{**}P < 0.01$.

pushes downwards, the transit amplifying zone pulls upwards and shears inwards, and the villus-like domain shears outwards.

**Crypt size and folding depend on substrate rigidity.** We next investigated how these mechanical compartments control the shape and function of the crypt and its transition towards the villus-like domain. Our measurements of normal tractions (Fig. 1e,f) suggest that the crypt folds by pushing the stem cell compartment towards the substrate, but folding was frustrated because the underlying substrate was too stiff. Thus, we investigated whether a sufficiently soft substrate would enable the stem cell compartment to adopt the folded shape characteristic of 3D organoids and in vivo crypts. To study the interplay between substrate stiffness, tractions and folding, we cultured intestinal organoids on substrates of varying stiffness, spanning nearly two orders of magnitude. On the stiffest substrate (15 kPa), the stem cell compartment bulged out of the monolayer (Fig. 2a). By contrast, when organoids were grown on progressively softer substrates, they showed an increasingly pronounced folding (Fig. 2a,b). We measured the cell tractions for each substrate stiffness except for the 0.2 kPa substrates, which displayed extreme deformations and hydrogel creasing instabilities that prevented an accurate calculation (Fig. 2a). The radial traction component was strongly dependent on the substrate stiffness, whereas the normal component was not (Fig. 2c,d). This observation prompted us to study whether the substrate stiffness influences epithelial compartmentalization. We found that the size of the stem cell compartment and the number of stem cells therein decreased as substrate stiffness increased (Fig. 3a–c). By contrast, the ratio of stem to Paneth cells was insensitive to stiffness (Fig. 3d). These experiments show that the mechanical microenvironment regulates intestinal homeostasis.

**The crypt folds through apical constriction.** Two classes of folding mechanisms can explain the observed traction patterns and monolayer geometry. The first class relies on differentials in mitotic pressure[8–10,33], which can induce a buckling instability that pushes the stem cell compartment towards the substrate. A second class is based on differentials in myosin contractility, either across the monolayer plane[12] or along the apicobasal axis[14–16]. To discriminate between these two classes of mechanisms, we treated cells with blebbistatin. Following the addition of increasing doses (0.5–15 μM) of this specific inhibitor of myosin II ATPase activity, the traction forces were progressively impaired and the monolayer flattened gradually

(Extended Data Fig. 2a–c). All traction forces vanished at a dose of 15 µM (Fig. 4a–c and Supplementary Video 7) and the crypt indentation was negligible (Fig. 4d,e). The elongated shape of the basal cell surface at the transit amplifying zone, which was unaffected by the stiffness of the gel, was largely lost by this treatment. When blebbistatin was washed out, the traction patterns re-emerged, the elongated morphology was recovered and the monolayer refolded (Fig. 4a–c and Extended Data Fig. 2d). Remarkably, the crypt size decreased after recovering from blebbistatin, further emphasizing a mechanical control of intestinal homeostasis (Fig. 4a,b).

To study how the actomyosin cytoskeleton drives crypt folding, we measured the distribution of actin and myosin across organoid monolayers seeded on stiff (5 kPa) and soft (0.7 kPa) substrates. Irrespective of the substrate stiffness, F-actin staining (phalloidin) and live imaging of organoids expressing myosin IIA–enhanced green fluorescent protein (eGFP) revealed an actomyosin accumulation at the apical surface of the stem cell compartment (Fig. 4f and Extended Data Figs. 2e, 3a,b). In addition, they showed a basal ring of circumferential stress fibres under the elongated cells at the transit amplifying zone. This actomyosin distribution suggests two potential mechanisms that are not mutually exclusive. The first is that myosin differentials across the apicobasal cell axis drive monolayer bending through apical constriction. The second is that supracellular contraction of the transit amplifying zone compresses the stem cell compartment radially to induce its buckling. To assess the contribution of bending versus buckling, we reasoned that both mechanisms involve cell–cell stresses of opposite sign. In the bending scenario, cells in the stem cell compartment should pull on each other differentially along the apicobasal axis to indent the substrate, thereby generating an apical tensile stress. By contrast, in the buckling scenario, cells in the stem cell compartment should push on each other as a result of the compressive stress generated by the contractile ring at the transit amplifying zone.

To measure the sign of the stress field, we performed circular laser ablations along the internal and external boundaries of the transit amplifying zone. In both cases ablations induced a radial recoil on both sides of the cuts (Fig. 4g, Extended Data Fig. 2f and Supplementary Videos 8–11). The recoils were asymmetrical and showed non-monotonic velocity fields, suggesting that monolayer friction and viscosity follow a complex spatial distribution that prevents a straightforward readout of the relative tensions from recoil dynamics (Fig. 4h and Extended Data Fig. 2g,h). However, the fact that monolayers recoiled on both sides of the cuts implies that the crypt is under tension. Moreover, after cutting the monolayer at the inner boundary of the transit amplifying zone, the stem cell compartment increased its indentation of the substrate (Fig. 4i). This set of experiments rules out compressive buckling driven by myosin differentials between crypt compartments or by mitotic pressure. It instead shows that the stem cell compartment bends by apical constriction.

**The actomyosin cortex determines cell shape and traction.** We next investigated how cell shape evolves between compartments (Fig. 5a–n). To this aim, we segmented individual cell shapes in crypts grown on stiff (15 kPa) and soft (0.7 kPa) substrates. The cell shapes were heterogeneous (Extended Data Fig. 4a and Supplementary Videos 12,13) but averages over all cells and crypts revealed consistent morphometric patterns (Fig. 5a,b). The apical area of the stem cells on both the stiff and soft substrates was smaller than the basal area (Fig. 5e,f). Paneth cells showed the opposite behaviour (Extended Data Fig. 4a–d), indicating that stem, but not Paneth, cells drive apical constriction of the stem cell compartment. Both cell types were taller than differentiated cells (Fig. 5g) and displayed an apicobasal tilt towards the centre of the crypt, which peaked at the boundary between the stem cell compartment and the transit amplifying zone (Fig. 5h). On reaching this boundary, the differences between the apical and basal area vanished and the cells became basally elongated along the circumferential direction (Fig. 5i). Treatment with blebbistatin for 3 h reduced the tilt at the stem cell compartment and the basal aspect ratio of every cell type at the crypt (Extended Data Fig. 5).

To investigate the link between tissue shape, cell shape, cell–ECM tractions and actomyosin localization, we developed a 3D vertex model[34–36] of the crypt coupled to a soft hyperelastic substrate (Supplementary Note 1 and Extended Data Fig. 6,7). We considered a uniform flat monolayer with a pattern of cell surface tensions as suggested by the measured distribution of cortical components (Fig. 4f and Extended Data Figs. 2e,3). Specifically, we prescribed apical and basal surface tensions with a profile following the measured F-actin density (Fig. 4f and Supplementary Note 1). We then allowed the monolayer to equilibrate its shape while adhering to the substrate. The model was able to recapitulate all morphological features of the monolayer—both at the cell and tissue scales—including cell height, shape and monolayer folding, for both soft and stiff substrates (Fig. 5c,d). The model captured apical constriction (Fig. 5j,k) and increased cell height (Fig. 5l) at the stem cell compartment, apicobasal cell tilt (Fig. 5m) and basal tangential elongation at the transit amplifying zone (Fig. 5n). Besides cell and tissue morphology, the model also predicted the distribution of normal cell-substrate tractions (Fig. 5o), from which we estimated a maximum apical tension of $4.6 \pm 1.7$ mN m$^{-1}$ (mean ± s.d.). The model also captured the local recoil of the monolayer following laser cuts (Fig. 5p,q). The overall agreement

**Fig. 4 | The crypt folds under tension generated by myosin II. a**, Traction maps under baseline conditions (left), after 3 h of blebbistatin treatment (centre) and after 11 h of blebbistatin washout (right) on 5 kPa substrates. Membrane-targeted tdTomato (medial plane; top). Three-dimensional traction maps (centre). The yellow vectors represent components tangential to the substrate; the colour map represents the component normal to the substrate. Lateral view along the crypt midline (bottom). Representative images of three independent experiments. **b**, Normal traction as a function of the distance to the crypt centre before, during and after blebbistatin treatment. **c**, Time evolution of normal traction for the stem cell compartment and transit amplifying zone before, during and after blebbistatin treatment. **b**,**c**, $n = 11$ samples from three independent experiments. **d**, Lateral views of crypts seeded on 0.7 kPa gels and treated with dimethylsulfoxide (top) or blebbistatin (bottom) for 3 h. **e**, Indentation at the centre of the crypt in cells treated with dimethylsulfoxide or blebbistatin for 3 h. $P < 0.0001$, two-tailed unpaired Student's $t$-test; $n = 12$ crypts from two independent experiments. **f**, F-actin (phalloidin) staining of crypts on 5 kPa gels. Projections of basal (left) and apical (centre) F-actin of a representative crypt. Lateral view of the same crypt (top right). Radial distribution of the apical and basal F-actin intensity as a function of the distance to the crypt centre (bottom right). $n = 36$ crypts from four independent experiments. **g**, Recoil-velocity maps immediately after ablation along the red lines of two crypts on 5 kPa substrates (bottom). Cut inside the transit amplifying zone (left). Cut outside the transit amplifying zone (right). The two crypts before ablation (top). **h**, Radial recoil velocity as a function of the distance to the crypt centre for cuts between the stem cell compartment and transit amplifying zone (green), and the transit amplifying zone and villus-like domain (blue); $n = 14$ (cut stem–TA) and 11 (cut TA–villus-like) crypts from five independent experiments. **i**, Indentation at the centre of the crypt before and after cutting between the stem cell compartment and the transit amplifying zone. $P = 0.0313$, two-tailed Wilcoxon paired test; $n = 6$ crypts from two independent experiments. **b**,**c**,**e**,**f**,**h**, Data are represented as the mean ± s.e.m. (**b**,**c**) or mean ± s.d. (**e**,**f**,**h**). **a**,**d**,**f**,**g**, Scale bars, 20 µm. Memb, membrane; TA, transit amplifying zone; DMSO, dimethylsulfoxide; bleb, blebbistatin; a.u., arbitrary units; $^{***}P < 0.001$ and $^{*}P < 0.05$.

between the model and experiments shows that a stereotyped contractility pattern in the crypt can explain its stiffness-dependent shape and normal traction patterns.

**Cell fate and mechanics co-evolve during crypt formation.** We next studied how this mechanical picture co-evolves with cell-fate specification during crypt formation. We treated 3D organoids with

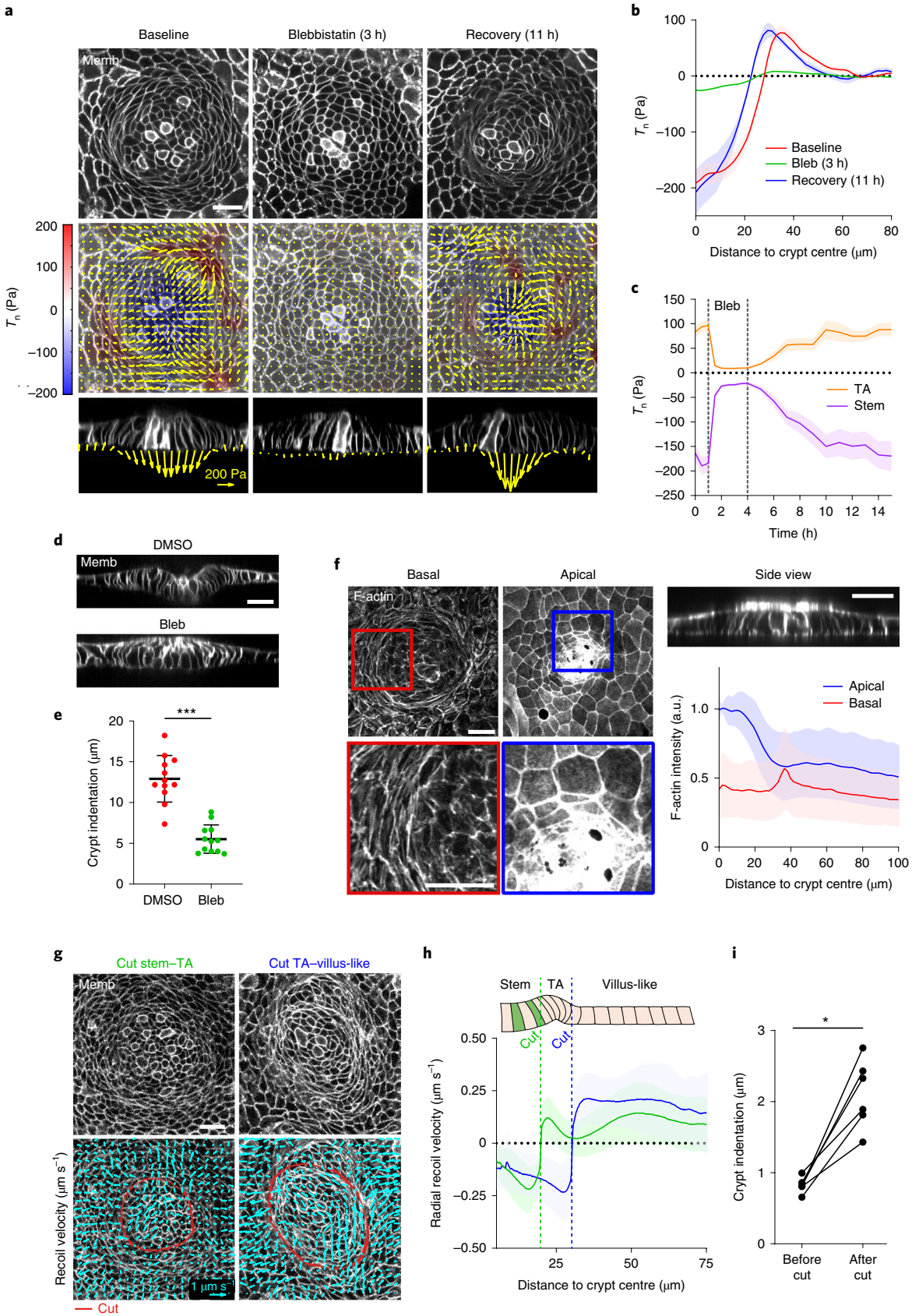

ENR medium containing CHIR99021 and nicotinamide for 48 h to mimic a hyperproliferative fetal progenitor state[37–39]. Following this treatment, the organoids lost their buds and formed cysts. We then dissociated the cysts and seeded the resulting cells at high density on soft two-dimensional (2D) substrates. The cells adhered readily, proliferated and progressively formed a confluent monolayer. This monolayer lacked the packing geometry, apical accumulation of actomyosin, traction compartmentalization and expression pattern of Olfm4 and cytokeratin 20 characteristic of crypts and villi. One day after replacing the culture medium with regular ENR, we observed the formation of cellular foci that expressed Olfm4, exhibited apical F-actin and myosin IIA, and generated downwards traction (Fig. 6a,b). The expression levels of Olfm4 inside the foci and cytokeratin 20 outside them increased steadily over the following days (Fig. 6c,d). The number foci was constant in time, and their size plateaued after 24 h (Fig. 6e,f). F-actin and myosin IIA increased over time at the apical and basal surfaces of both the crypt and the villus-like compartments (Fig. 6g and Extended Data Fig. 8a–c). Although the apical actin and myosin densities at the stem cell compartment were the highest across the monolayer, their ratio to the basal densities decreased with time (Fig. 6h and Extended Data Fig. 8d). However, the normal forces at the centre of the stem cell compartment increased, probably because of the rise in the total amount of actomyosin (Fig. 6i). These experiments show that apical constriction and pushing forces arise as early as the time at which Olfm4 foci can be detected (day 2), before crypt size and density in the monolayer are established (day 3). Forces thus co-evolve with fate specification to progressively shape a mature compartmentalized epithelium.

**Comparison with the intestinal epithelium in vivo.** To assess whether our organoids captured the cellular morphology and cytoskeletal organization of the in vivo crypt and villus, we studied whole-mount sections of the small intestine of mice. We focused on myosin IIA to avoid the confounding contribution of non-contractile F-actin at the brush border (Fig. 7a). Apical myosin IIA was highest at the stem cell compartment and dropped at the villus. By contrast, basal myosin IIA increased progressively from the base of the crypt towards the villus, where the presence of stromal cells prevented further quantification (Fig. 7b,c). The cells at the base of the crypt were slightly tilted towards the villus. This tilt is in the opposite direction to that observed in our organoids, showing that besides active processes, tilting is influenced by curvature and spatial constrains[40]. Beyond this highly curved region, the cells were tilted towards the crypt centre, in agreement with our observations in organoids (Fig. 7d,e). Together, these data reveal a substantial agreement between organoids and the intestinal epithelium.

**Cells are dragged out of the crypt.** We next studied the dynamics of the cell monolayer. Cell movements at the villus are driven by active migration[41] but the mechanisms driving movements from the crypt to the villus remain unknown. The widely assumed mechanism for such movements, a pushing force arising from compression downstream of mitotic pressure[42,43], is incompatible with our observation that the transit amplifying zone is under tension. To study the mechanisms underlying cell movements, we studied maps of cell velocities and forces in the organoid monolayers (Fig. 8a–j). Particle imaging velocimetry (PIV) on 5 kPa gels revealed strong spatial fluctuations in cell velocities, characterized by clusters of fast-moving cells surrounded by nearly immobile ones (Fig. 8a and Supplementary Video 14). To average out these fluctuations and unveil systematic spatio–temporal patterns, we computed the average radial velocity as a function of the distance from the crypt centre. Kymograph representation of this average showed that the radial velocity was weak in the central region of the stem cell compartment, begun to increase near the transit amplifying zone and peaked at the boundary with the villus-like domain (Fig. 8c,i). The cell division rate followed an opposite profile characterized by a plateau at the stem cell compartment and a decrease thereafter.

To understand how the spatial distribution of cell velocity arises from cellular forces, we turned to kymographs of radial cell–ECM tractions and radial cell–cell monolayer tension measured using monolayer stress microscopy (Supplementary Note 2)[44]. Similar to the velocity kymographs, the traction and tension kymographs were stationary, confirming that our 2D organoids are in steady state within our window of observation (Fig. 8d,e). Kymographs of the radial tractions displayed the three compartments already shown in Fig. 1e; in the stem cell compartment the radial tractions pointed inwards, in the transit amplifying zone they vanished, and in the villus-like domain they pointed outwards (Fig. 8i). By contrast, kymographs of the cell–cell tension showed a minimum at the transit amplifying zone flanked by two tension gradients that built up towards the centre of the crypt and towards the villus-like domain (Fig. 8e,i).

We repeated this set of experiments on softer substrates (0.7 kPa; Fig. 8b and Supplementary Video 15), which showed similar cell velocity profiles to those obtained on the 5 kPa substrates (Fig. 8f–h,j). In this compartment, the radial tractions were nearly one order of magnitude weaker than on the 5 kPa substrates. Close to the transit amplifying zone, the radial tractions changed direction and displayed a positive peak of similar magnitude but shorter length than on the 5 kPa substrates. The pronounced negative gradient in tension observed at the stem cell compartment on the 5 kPa substrates nearly vanished on the 0.7 kPa substrates. However, we found a positive tension gradient that begins at the boundary of

**Fig. 5 | Crypts fold through apical constriction. a**,**b**, Three-dimensional crypt segmentation on stiff (**a**; 15 kPa) and soft (**b**; 0.7 kPa) substrates. Representative of three crypts per stiffness from two (0,7 kPa) and three (15 kPa) independent experiments. Colors indicate different cells. **c**,**d**, Three-dimensional vertex model of a monolayer adhered to a stiff (**c**) and soft (**d**) substrate. The colours in the cell outlines indicate the surface tension. **e**,**f**, Apical and basal area profiles on stiff (**e**; 15 kPa) and soft (**f**; 0.7 kPa) substrates. Paneth cells were excluded from the analysis (see Extended Data Fig. 4). From the centre to the edge bins, $n = 77$, 198, 339 and 307 cells for **f**, and 32, 61, 102 and 230 for **e** from two and three independent experiments, respectively. **g**–**i**, Cell height (**g**), apicobasal tilt (**h**) and basal aspect ratio (**i**) as a function of the distance to the crypt centre on soft and stiff substrates. Paneth cells were excluded from the analysis of the tilt and aspect ratio (see Extended Data Fig. 4). The vertical dashed lines indicate the boundary between the stem cell compartment and transit amplifying zone, and the transit amplifying zone and villus-like domain (in **g**). The crypts and number of cells are the same as for **e** (15 kPa) and **f** (0.7 kPa). For the cell-height profiles: from centre to edge bins, $n = 77$, 198, 339, 307, 242, 192 and 159 cells for the soft substrates, and $n = 32$, 61, 102, 230, 165, 125 and 106 cells for the stiff substrates. **j**,**k**, Simulated apical and basal area profiles on a rigid (**j**) and soft (**k**) substrate. From the centre to the edge bins, $n = 9$, 26, 54 and 230 simulated cells for **k**, and $n = 10$, 28, 54 and 227 simulated cells for **j**. **e**–**k**, Data are represented as the mean ± s.e.m. **l**–**n**, Simulated cell height (**l**), apicobasal tilt (**m**) and basal aspect ratio (**n**) on soft and rigid substrates. The crypts are the same as for **j**,**k**. **o**, Simulated normal traction. **p**, Simulated tissue recoil after laser ablations (red) at the boundary between the stem cell compartment and transit amplifying zone (left), and the transit amplifying zone and villus-like domain (right). The cyan vectors indicate tissue displacement right after ablation. **q**, Radial displacement in the two simulated cuts. Data are represented as the mean ± s.d. The vertical dashed lines indicate cuts. **a**,**b**,**p**, Scale bars, 20 μm. Memb, membrane; TA, transit amplifying zone; and a.u., arbitrary units.

the stem cell compartment, persists through the transit amplifying zone, and decays thereafter. Thus, despite large quantitative differences at the stem cell compartment on soft and stiff substrates, the radial tractions on both substrates displayed a region where they changed sign and pointed away from the crypt centre, resulting in a positive tension gradient.

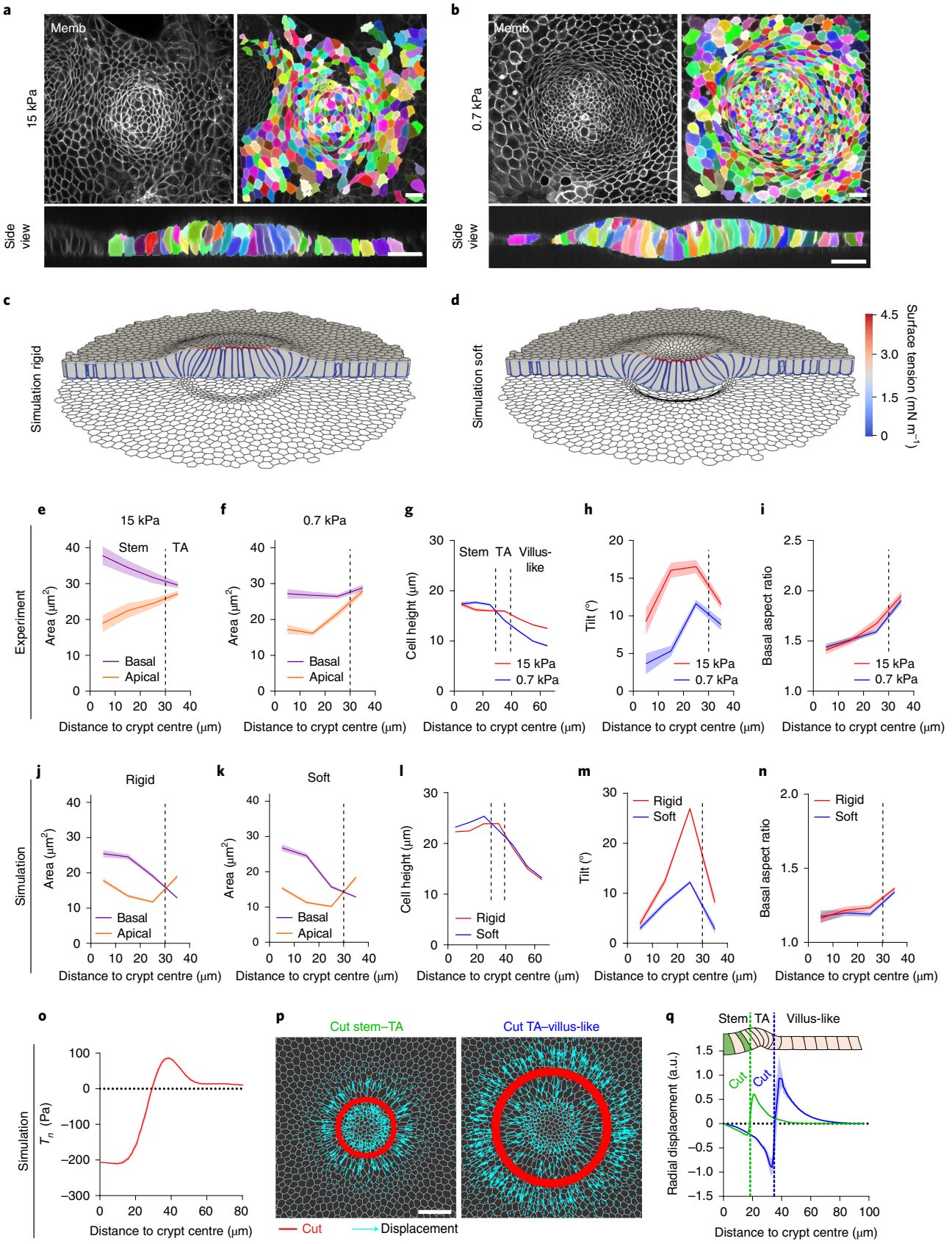

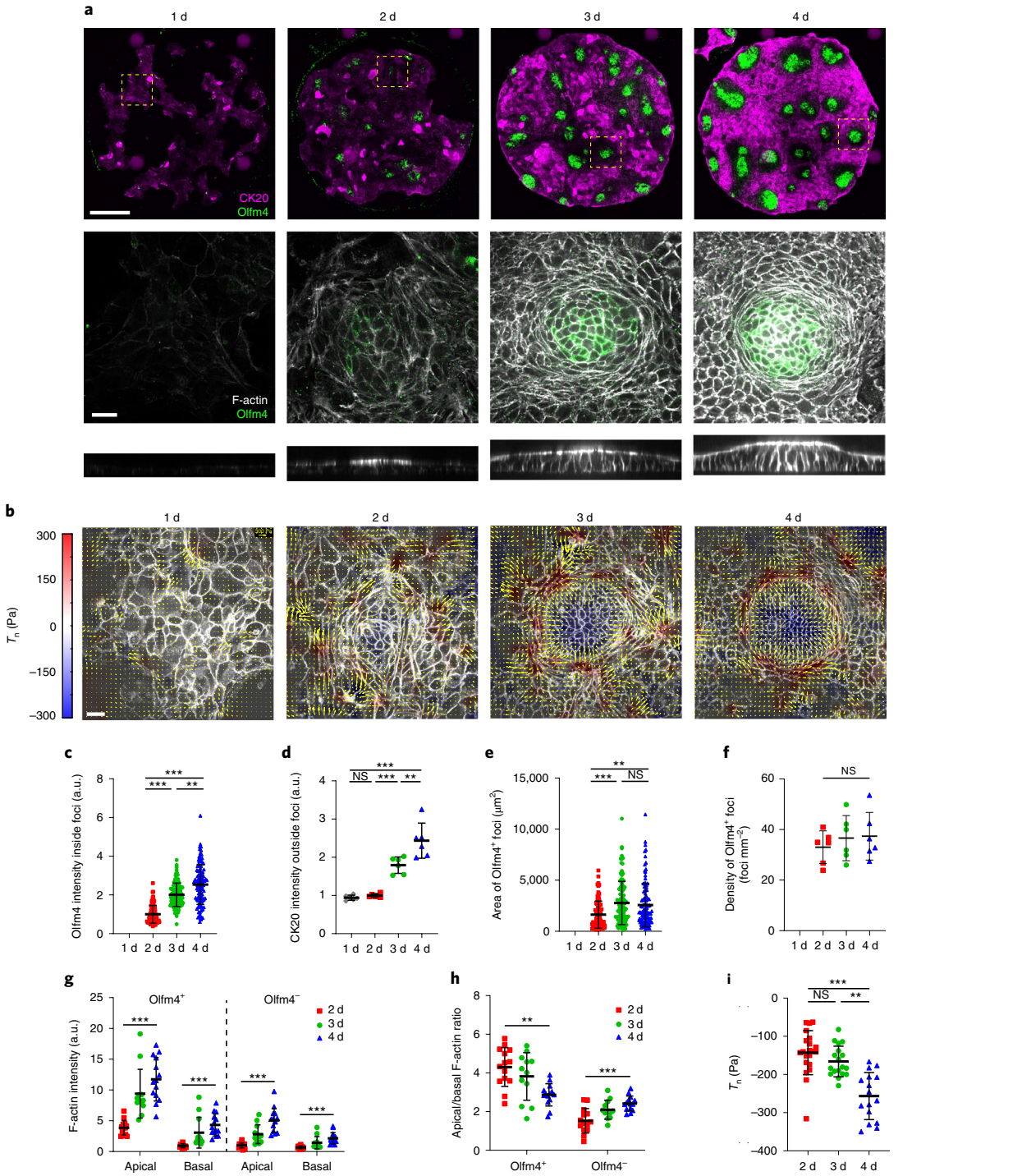


**Fig. 6 | Co-evolution of cell fate and tissue mechanics during de novo crypt formation. a**, Olfm4 and cytokeratin 20 immunostaining following the development of the monolayers over four consecutive days (top). F-actin (phalloidin) and Olfm4 immunostaining (middle), and lateral views of F-actin (bottom) at the positions indicated with a dashed square in the corresponding monolayers of the top row. Scale bars, 200 μm (top) and 20 μm (bottom). **b**, Three-dimensional tractions at the indicated time points. The yellow vectors represent components tangential to the substrate and the colour map represents the component normal to the substrate. Scale bar, 20 μm. **a**,**b**, Representative images of two independent experiments. **c**–**f**, Olfm4 intensity inside the Olfm4$^+$ foci (**c**), cytokeratin 20 intensity in the Olfm4$^-$ regions (**d**), area of the Olfm4$^+$ foci (**e**) and density of the Olfm4$^+$ foci (**f**) at the indicated time points; $n = 90$ (2 d), 112 (3 d) and 115 (4 d) Olfm4$^+$ foci (**c**,**e**), and $n = 6$ (1, 2, 3 and 4 d) circular patterns (**d**,**f**) from two independent experiments. **g**,**h**, Apical and basal F-actin intensity (**g**) and apical/basal F-actin ratio (**h**) in the Olfm4$^+$ and Olfm4$^-$ regions for the indicated time points; $n = 14$ (2 d), 12 (3 d) and 14 (4 d) crypts from two independent experiments. Only the statistical comparisons between 2 d and 4 d are shown. **i**, Mean normal traction at the stem cell compartment for the indicated time points; $n = 21$ (2 d), 18 (3 d) and 16 (4 d) crypts from two independent experiments. **c**–**i**, Data are represented as the mean ± s.d. Statistical significance was determined using a Kruskal–Wallis test, followed by a Dunn's multiple-comparison test (**c**,**e**,**i**,**g** and **h** for Olfm4$^+$), and a one-way analysis of variance, followed by a Tukey's multiple-comparison test (**d**,**f** and **h** for Olfm4$^-$); $^*P < 0.05$; $^{**}P < 0.01$; $^{***}P < 0.001$; and NS, not significant ($P > 0.05$). CK20, cytokeratin 20; and a.u., arbitrary units.

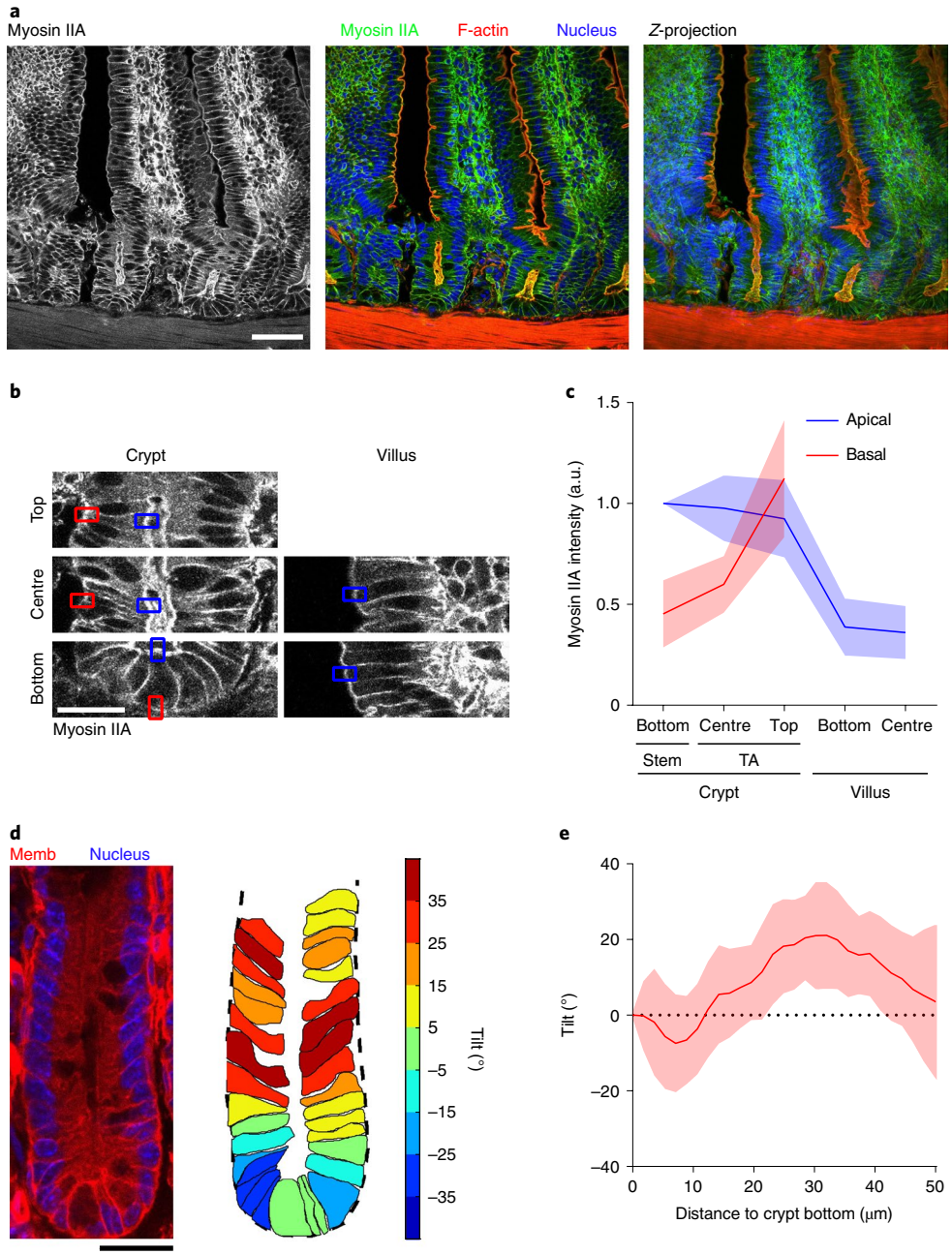


**Fig. 7 | Cell morphology and cytoskeletal organization of the intestinal epithelium in vivo. a**, Staining of F-actin (phalloidin) and nuclei (4,6-diamidino-2-phenylindole, DAPI) of tissue sections of the small intestine of myosin IIA–eGFP mice. Myosin IIA–eGFP signal (left). Overlay of myosin IIA–eGFP, F-actin and nuclei (centre). Maximum intensity *z*-projection of the overlayed channels to better visualize the continuity of the crypt–villus axis (right). Scale bar, 40 μm. **b**, Illustration of the approach used to quantify the myosin IIA intensity along the crypt–villus axis in tissue sections. The myosin intensity was measured at the basal (red) and apical (blue) sides of cells at the indicated crypt and villus regions. Note that the high myosin IIA intensity of stromal cells prevented accurate quantification of the basal epithelial intensity at the villus. **a**,**b**, Representative images of 13 crypt–villus units from three mice. **c**, Apical and basal myosin IIA distribution along the crypt–villus axis of tissue sections. Data are represented as the mean ± s.d. of $n = 13$ crypt–villus units from three mice; a.u., arbitrary units. **d**, Example of an intestinal crypt from membrane–tdTomato mice (left). The membrane signal (Memb) has been overlaid on the nuclear signal (DAPI). Representative image of 16 crypts from three mice. Cell segmentation of the same crypt (right). The basal contour of the crypt is delineated with a black dashed line. Individual cells are coloured according to their tilting angle with respect to the normal direction to the crypt contour (positive indicates towards the crypt bottom; negative indicates away from the crypt bottom). **b**,**d**, Scale bars, 20 μm. **e**, Cell tilt along the crypt axis. Data are represented as the mean ± s.d. of $n = 16$ crypts from three mice.

To further substantiate this tensional landscape, we again resorted to laser ablation but this time we cut the monolayer radially. As commonly observed in laser ablation experiments, we found recoil perpendicular to the cut (Fig. 8k–m and Supplementary Videos 16,17). Surprisingly, however, the dominant recoil component was parallel to the cut. This radial recoil was minimum at the boundary

between the crypt and the villus-like domain and increased on either side of it. Our vertex model predicts radial recoil at the stem cell compartment as a consequence of apical constriction but not at the villus-like domain. Recoil in this domain is consistent with a tensile gradient associated with migratory forces that pull cells out of the crypt, which are not included in our model.

**Fig. 8 | Cells are dragged out of the crypt towards the villus-like domain. a**,**b**, Representative velocity maps (right) overlaid on membrane-targeted tdTomato signal (Memb; left) on 5 kPa (**a**) and 0.7 kPa (**b**) substrates. Representative images of five crypts from three independent experiments (**a**) and seven crypts from two independent experiments (**b**). Memb, membrane; Scale bars, 40 μm. **b**, Due to pronounced crypt folding, for visualization purposes, the image for the 0.7 kPa substrate is a projection along the crypt medial plane. **c**–**h**, Kymographs showing the circumferentially averaged radial velocity (**c**,**f**), radial traction (**d**,**g**) and radial tension (**e**,**h**) on 5 kPa (**c**–**e**) and 0.7 kPa (**f**–**h**) substrates for 6.5 h. The vertical dashed line indicates the boundary between the stem cell compartment and the transit amplifying zone. **i**,**j**, Time-averaged radial profiles of the traction, tension, velocity and cell division rate on 5 kPa (**i**) and 0.7 kPa (**j**) substrates. The vertical dashed line indicates the boundary between the stem cell compartment and the transit amplifying zone. **c**–**j**, Data are represented as the mean ± s.e.m. of $n = 5$ crypts from three independent experiments (**c**–**e**,**i**) and $n = 7$ crypts from two independent experiments (**f**–**h**,**j**). Note that for an unbounded monolayer, monolayer stress microscopy computes stress up to a constant (Supplementary Note 2). As the laser cuts indicated tension everywhere in the monolayer, this constant was arbitrarily set so that the minimum tension throughout the time lapse was zero. **k**–**m**, Recoil velocity maps (top), and the parallel and perpendicular velocity (bottom) immediately after laser ablation along the crypt–villus axis on 5 kPa (**k**) and 0.7 kPa (**l**) substrates, and simulations (**m**). The red lines indicate the ablated area. The yellow dashed lines indicate the crypt contours. Data are represented as the mean ± s.d. of $n = 11$ crypts from three independent experiments (**k**) and $n = 13$ crypts from four independent experiments (**l**). Scale bars, 20 μm.

Together, our data indicate that cells exit the crypt using a collective cell-migration mode in which cell velocity is parallel to cell-substrate traction, rather than antiparallel to it. This alignment is opposite to that observed at the leading edge of advancing monolayers[45,46]. Because cells are under tension, outward-pointing tractions cannot arise from pushing forces generated at the stem cell compartment. Our evidence instead indicates that cells at the crypt are dragged by other cells located further into the villus-like domain, much as the trailing edge of a cell cluster is dragged by the leading edge[47]. Thus, the boundary of the crypt can be understood as a multicellular trailing edge that is constantly being replenished with cells through proliferation.

## Discussion

Organoid biology has revolutionized life sciences by providing accessible systems to study the interplay between tissue fate, form and function. Mechanics plays a central role in this interplay[48–51] but our understanding of organoid mechanobiology has been impaired by the lack of approaches to map cellular forces in organoids. Traction maps can be obtained in organoids surrounded by 3D ECM but their resolution and accuracy are strongly limited by the nonlinearity of the ECM, its degradability and limited optical accessibility of the sample[24,52]. Here we presented mechanically accessible intestinal organoids that enable time-lapse force mapping with sub-cellular resolution. Besides enabling direct force mapping, our organoid monolayers offer several advantages over traditional 3D organoids surrounded by ECM. These advantages include versatile control of the mechanical environment, straightforward optical access and an open lumen that better mimics the open-tube configuration of gut and prevents the unphysiological accumulation of extruded cells[26–31]. Moreover, cells in our organoids exhibit a collective migratory pattern from the crypt to the villus, a feature that is not well captured by traditional 3D organoids. Similar to other organoid models, our system misses some features of the in vivo epithelium. Limitations include that the transit amplifying zone is shorter than in vivo, the villus geometry is not recapitulated, and cells in the villus-like domain are thinner than in vivo and lack a well-developed brush border.

Direct access to cellular forces allowed us to identify mechanical compartments in which cell-substrate tractions, monolayer stresses and their spatial derivatives differ in magnitude and sign. We showed how these compartmentalized mechanical variables enable both tissue folding and collective cell migration. In an accompanying paper, Yang et al.[53] studied the mechanics of crypt morphogenesis in intestinal organoids enclosing a pressurized lumen. In agreement with our results, they report apical constriction of stem cells (but not Paneth cells) and basal constriction beyond the boundary of the niche. They also report a contribution of volume changes in enterocytes, which we did not address in our study. We note that our finding that the stem cell compartment folds further when separated from the rest of the epithelium (Fig. 4i), indicates that basal accumulation of actomyosin at the villus or changes in volume in enterocytes are dispensable for folding. Both studies reveal the potential of organoid systems to study the mechanobiological principles of gut epithelial shape and compartmentalization. These approaches can also be applied to study the role of mechanics in other key processes in intestinal physiology and disease, such as proliferation, differentiation, inflammation, regeneration and malignancy.

## Online content

Any methods, additional references, Nature Research reporting summaries, source data, extended data, supplementary information, acknowledgements, peer review information; details of author contributions and competing interests; and statements of data and code availability are available at https://doi.org/10.1038/s41556-021-00699-6.

Received: 17 July 2020; Accepted: 12 May 2021;
Published online: 21 June 2021

## References

1. Chacón-Martínez, C. A., Koester, J. & Wickström, S. A. Signaling in the stem cell niche: regulating cell fate, function and plasticity. *Development* **145**, dev165399 (2018).
2. Barker, N. et al. Identification of stem cells in small intestine and colon by marker gene *Lgr5*. *Nature* **449**, 1003–1007 (2007).
3. Ritsma, L. et al. Intestinal crypt homeostasis revealed at single-stem-cell level by in vivo live imaging. *Nature* **507**, 362–365 (2014).
4. Snippert, H. J. et al. Intestinal crypt homeostasis results from neutral competition between symmetrically dividing Lgr5 stem cells. *Cell* **143**, 134–144 (2010).
5. Shyer, A. E. et al. Villification: how the gut gets its villi. *Science* **342**, 212–218 (2013).
6. Hughes, A. J. et al. Engineered tissue folding by mechanical compaction of the mesenchyme. *Dev. Cell* **44**, 165–178 (2018).
7. Walton, K. D. et al. Hedgehog-responsive mesenchymal clusters direct patterning and emergence of intestinal villi. *Proc. Natl Acad. Sci. USA* **109**, 15817–15822 (2012).
8. Hannezo, E., Prost, J. & Joanny, J. F. Instabilities of monolayered epithelia: shape and structure of villi and crypts. *Phys. Rev. Lett.* **107**, 078104 (2011).
9. Almet, A. A., Maini, P. K., Moulton, D. E. & Byrne, H. M. Modeling perspectives on the intestinal crypt, a canonical system for growth, mechanics, and remodeling. *Curr. Opin. Biomed. Eng.* **15**, 32–39 (2020).
10. Tozluoğlu, M. et al. Planar differential growth rates initiate precise fold positions in complex epithelia. *Dev. Cell* **51**, 299–312 (2019).
11. Drasdo, D. Buckling instabilities of one-layered growing tissues. *Phys. Rev. Lett.* **84**, 4244–4247 (2000).
12. Chung, S. Y., Kim, S. & Andrew, D. J. Uncoupling apical constriction from tissue invagination. *eLife* **6**, e22235 (2017).
13. Sanchez-Corrales, Y. E., Blanchard, G. B. & Röper, K. Radially patterned cell behaviours during tube budding from an epithelium. *eLife* **7**, e35717 (2018).
14. Sumigray, K. D., Terwilliger, M. & Lechler, T. Morphogenesis and compartmentalization of the intestinal crypt. *Dev. Cell* **45**, 183–197 (2018).

15. Martin, A. C. & Goldstein, B. Apical constriction: themes and variations on a cellular mechanism driving morphogenesis. *Development* **141**, 1987–1998 (2014).
16. Sui, L. et al. Differential lateral and basal tension drive folding of *Drosophila* wing discs through two distinct mechanisms. *Nat. Commun.* **9**, 4620 (2018).
17. Nelson, C. M. et al. Microfluidic chest cavities reveal that transmural pressure controls the rate of lung development. *Development* **144**, 4328–4335 (2017).
18. Latorre, E. et al. Active superelasticity in three-dimensional epithelia of controlled shape. *Nature* **563**, 203–208 (2018).
19. Sato, T. et al. Single Lgr5 stem cells build crypt-villus structures in vitro without a mesenchymal niche. *Nature* **459**, 262–265 (2009).
20. Spence, J. R. et al. Directed differentiation of human pluripotent stem cells into intestinal tissue in vitro. *Nature* **470**, 105–110 (2011).
21. Sato, T. & Clevers, H. Growing self-organizing mini-guts from a single intestinal stem cell: mechanism and applications. *Science* **340**, 1190–1194 (2013).
22. Gjorevski, N. et al. Designer matrices for intestinal stem cell and organoid culture. *Nature* **539**, 560–564 (2016).
23. McKinley, K. L. et al. Cellular aspect ratio and cell division mechanics underlie the patterning of cell progeny in diverse mammalian epithelia. *eLife* **7**, e36739 (2018).
24. Broguiere, N. et al. Growth of epithelial organoids in a defined hydrogel. *Adv. Mater.* **30**, e1801621 (2018).
25. Pérez-González, C. et al. Active wetting of epithelial tissues. *Nat. Phys.* **15**, 79–88 (2019).
26. Thorne, C. A. et al. Enteroid monolayers reveal an autonomous WNT and BMP circuit controlling intestinal epithelial growth and organization. *Dev. Cell* **44**, 624–633 (2018).
27. Altay, G. et al. Self-organized intestinal epithelial monolayers in crypt and villus-like domains show effective barrier function. *Sci. Rep.* **9**, 10140 (2019).
28. Liu, Y., Qi, Z., Li, X., Du, Y. & Chen, Y. G. Monolayer culture of intestinal epithelium sustains Lgr5$^+$ intestinal stem cells. *Cell Disco.* **4**, 32 (2018).
29. Kasendra, M. et al. Development of a primary human Small Intestine-on-a-Chip using biopsy-derived organoids. *Sci. Rep.* **8**, 2871 (2018).
30. Verhulsel, M. et al. Developing an advanced gut on chip model enabling the study of epithelial cell/fibroblast interactions. *Lab Chip* **21**, 365–377 (2021).
31. Nikolaev, M. et al. Homeostatic mini-intestines through scaffold-guided organoid morphogenesis. *Nature* **585**, 574–578 (2020).
32. Maskarinec, S. A., Franck, C., Tirrell, D. A. & Ravichandran, G. Quantifying cellular traction forces in three dimensions. *Proc. Natl Acad. Sci. USA* **106**, 22108–22113 (2009).
33. Trushko, A. et al. Buckling of an epithelium growing under spherical confinement. *Dev. Cell* **54**, 655–668 (2020).
34. Merkel, M. & Manning, M. L. A geometrically controlled rigidity transition in a model for confluent 3D tissues. *New J. Phys.* **20**, 022002 (2018).
35. Alt, S., Ganguly, P. & Salbreux, G. Vertex models: from cell mechanics to tissue morphogenesis. *Philos. Trans. R. Soc. B* **372**, 20150520 (2017).
36. Hannezo, E., Prost, J. & Joanny, J. F. Theory of epithelial sheet morphology in three dimensions. *Proc. Natl Acad. Sci. USA* **111**, 27–32 (2014).
37. Van Lidth de Jeude, J. F., Vermeulen, J. L. M., Montenegro-Miranda, P. S., Van den Brink, G. R. & Heijmans, J. A protocol for lentiviral transduction and downstream analysis of intestinal organoids. *J. Vis. Exp.* **98**, e52531 (2015).
38. Sato, T. et al. Paneth cells constitute the niche for Lgr5 stem cells in intestinal crypts. *Nature* **469**, 415–418 (2011).
39. Rodríguez-Colman, M. J. et al. Interplay between metabolic identities in the intestinal crypt supports stem cell function. *Nature* **543**, 424–427 (2017).
40. Rupprecht, J. F. et al. Geometric constraints alter cell arrangements within curved epithelial tissues. *Mol. Biol. Cell* **28**, 3582–3594 (2017).
41. Krndija, D. et al. Active cell migration is critical for steady-state epithelial turnover in the gut. *Science* **365**, 705–710 (2019).
42. Parker, A. et al. Cell proliferation within small intestinal crypts is the principal driving force for cell migration on villi. *FASEB J.* **31**, 636–649 (2017).
43. Clevers, H. The intestinal crypt, a prototype stem cell compartment. *Cell* **154**, 274–284 (2013).
44. Tambe, D. T. et al. Collective cell guidance by cooperative intercellular forces. *Nat. Mater.* **10**, 469–475 (2011).
45. Trepat, X. et al. Physical forces during collective cell migration. *Nat. Phys.* **5**, 426–430 (2009).
46. Du Roure, O. et al. Force mapping in epithelial cell migration. *Proc. Natl Acad. Sci. USA* **102**, 2390–2395 (2005).
47. Theveneau, E. et al. Chase-and-run between adjacent cell populations promotes directional collective migration. *Nat. Cell Biol.* **15**, 763–772 (2013).
48. Engler, A. J., Sen, S., Sweeney, H. L. & Discher, D. E. Matrix elasticity directs stem cell lineage specification. *Cell* **126**, 677–689 (2006).
49. Chan, C. J. et al. Hydraulic control of mammalian embryo size and cell fate. *Nature* **571**, 112–116 (2019).
50. Nelson, C. M., VanDuijn, M. M., Inman, J. L., Fletcher, D. A. & Bissell, M. J. Tissue geometry determines sites of mammary branching morphogenesis in organotypic cultures. *Science* **314**, 298–300 (2006).
51. McBeath, R., Pirone, D. M., Nelson, C. M., Bhadriraju, K. & Chen, C. S. Cell shape, cytoskeletal tension, and RhoA regulate stem cell lineage commitment. *Dev. Cell* **6**, 483–496 (2004).
52. Legant, W. R. et al. Measurement of mechanical tractions exerted by cells in three-dimensional matrices. *Nat. Methods* **7**, 969–971 (2010).
53. Yang, Q. et al. Cell fate coordinates mechano-osmotic forces in intestinal crypt morphogenesis. *Nat. Cell Biol.* https://doi.org/10.1038/s41556-021-00700-2 (2021).

## Methods

**Intestinal crypt isolation and organoid culture.** Animal experimentation was approved by the Animal care and Use Committee of Barcelona Science Park (CEEA-PCB) and Animal Welfare Body, Research Centre, Institut Curie. All procedures were carried out in compliance with the European Regulation for the Protection of Vertebrate Animals used for Experimental and other Scientific Purposes (Directive 2010/63).

Mice were housed with a 12-h dark–light cycle at 20 ± 4 °C and 20–85% humidity. Intestinal crypts from mT/mG[54], LifeAct–eGFP[55], myosin IIA–eGFP[56] and Lgr5–eGFP-IRES-CreERT2 (ref. [2]) male and female mice (3–6 months old) were isolated as described elsewhere[19]. The duodenum was isolated, washed in PBS and cut longitudinally. Villi were mechanically removed with a scalpel. The tissue was then dissociated in HBSS solution (Gibco) containing 8 mM EDTA (Sigma-Aldrich) for 20 min at 4 °C. After vigorous shaking, the solution was filtered through a 70-µm-pore cell strainer (Corning), obtaining the crypt fraction. The dissociation, shaking and filtration steps were repeated three times to increase the isolation yield. The final solution was centrifuged at 100*g* for 5 min at room temperature (RT), and the pellet containing crypts was resuspended in 1:1 Matrigel (Corning):ENR medium and seeded in drops of 50 µl in 24-well plates. After incubation for 25 min at 37 °C and 5% $CO_2$ in a humified atmosphere, the drops were covered with ENR medium. The organoids were split every 3–4 d. For splitting, the organoid-containing drops were mechanically disaggregated by pipetting in PBS supplemented with calcium and magnesium (Sigma-Aldrich), and centrifuged at 100*g* at RT for 3.5 min. The pellet was resuspended in 1:1 Matrigel:ENR and seeded in drops as explained above.

The ENR medium was composed of DMEM/F-12 medium (Gibco) supplemented with 2% antibiotic–antimycotic (Gibco), 2.5% GlutaMAX (Gibco), 20 ng ml$^{-1}$ mouseEGF (Peprotech), 100 ng ml$^{-1}$ noggin (Peprotech), 500 ng ml$^{-1}$ R-spondin1 (R&D Systems), 10 ng ml$^{-1}$ mouse FGF (Peprotech), 1×B-27 (Gibco) and 1×N-2 (Gibco).

**PAA gel polymerization.** Glass-bottom dishes (MatTek) were incubated for 10 min at RT with Bind-silane (Sigma-Aldrich) dissolved in absolute ethanol (PanReac) and acetic acid (Sigma-Aldrich) at volume proportions of 1:12:1. After two washes with absolute ethanol, 22.5 µl of the PAA mix (see Supplementary Table 1 for the different recipes used) were added on top of the glass and covered with an 18-mm coverslip. For the traction measurements, we used FluoSpheres with a diameter of 0.2 µm (Thermo Fisher Scientific). For immunostainings, we used CML latex beads with a diameter of 0.2 µm (Thermo Fisher Scientific). After 1 h polymerization at RT, PBS was added and the coverslips were removed with a scalpel.

**PAA gel functionalization and ECM micropatterning.** Organoid monolayers were confined in large circular ECM micropatterns (>900 µm). For this, the PAA gels were functionalized with 2 mg ml$^{-1}$ Sulpho-SANPAH (Cultek) irradiated for 7.5 min with ultraviolet light (365 nm). The gels were then washed twice with 10 mM HEPES (Gibco). For ECM micropatterning, polydimethylsiloxane (PDMS) stencils with circular openings were used[25]. The PDMS stencils were incubated with 2% pluronic acid F127 in PBS (Sigma-Aldrich) for 1 h. They were then washed twice with PBS and allowed to dry at RT for 20 min. The stencils were carefully placed on top of the functionalized PAA gels. A solution of 250 µg ml$^{-1}$ rat-tail type I collagen (First Link UK) and 100 µg ml$^{-1}$ laminin 1 (Sigma-Aldrich) dissolved in PBS was added on top of the PDMS stencils and incubated overnight at 4 °C. Finally, the ECM solution was aspirated, the gels were washed twice with PBS and the PDMS stencils were carefully removed.

**Seeding on PAA substrates.** The 3D intestinal organoids were mechanically disaggregated by pipetting in PBS containing calcium and magnesium (Sigma-Aldrich). For one PAA gel, we seeded the number of organoids contained in one Matrigel drop of the 24-well plate. After disaggregation, the organoids were centrifuged at 100*g* for 3.5 min at RT and the pellet was resuspended in ENR medium. The organoids were seeded in a small volume (50 µl) on top of the ECM-coated PAA gels and incubated at 37 °C and 5% $CO_2$. After incubation for 1 h, 550 µl ENR medium was added on top of the previous 50 µl. All experiments were performed 2–4 d after seeding.

**Immunostaining.** The organoid monolayers were fixed in 4% paraformaldehyde (PFA; Electron Microscopy Sciences) for 10 min at RT and washed three times with PBS. The samples were permeabilized with 0.1% Triton X-100 (Sigma-Aldrich) for 10 min at RT. After three washes with PBS, the samples were blocked with PBS containing 10% fetal bovine serum (Gibco) for 1 h at RT. Primary antibodies diluted in PBS containing 10% fetal bovine serum were added and incubated overnight at 4 °C. After three more washes in PBS, secondary antibodies and phalloidin in PBS containing 10% fetal bovine serum were added for 1 h at RT. Finally, the samples were washed five times with PBS (5 min each) and imaged.

For the immunostaining of tissue slices, adult (3–6 months old) R26$^{mT/mG}$ [54] or myosin IIA–GFP[56] mice were killed to isolate the small intestine (jejunum). After gently flushing the gut lumen with PBS, the tissue was hand cut into fragments that were 0.5–1 cm in length with a scalpel and fixed in 4% PFA (Electron Microscopy Sciences) for 1 h at RT. The tissue was then rinsed with PBS and either hand cut with a scalpel into approximately 1-mm-thick slices or embedded in 4% wt/vol low-melting point agarose (Ultrapure, Thermo Fisher) and transversally sectioned on a vibratome (Leica VT1000) to obtain gut slices that were approximately 350 µm thick. The slices were permeabilized with 1% Triton X-100 (Sigma-Aldrich) in PBS for 1 h at RT. All antibody solutions and wash steps were performed using 0.2% Triton X-100 in PBS on a shaker, with mild rocking. Incubations with primary antibodies were performed overnight at RT and were followed by three washes of 1 h each. Secondary antibodies and DAPI were added with or without phalloidin—all of which were diluted 1:200 in 0.2% Triton X-100 in PBS—and incubated overnight at 4 °C. After the washes (as described above), the samples were mounted on slides using mounting agent (aqua-poly/mount; Polysciences) and left to cure overnight at RT in the dark.

**Antibodies.** The primary antibodies used and their respective dilutions were: rabbit anti-Olfm4, 1:200 (Cell Signaling Technology, cat. no. 39141); mouse anti-CK20, 1:50 (Dako, cat. no. M7019); mouse anti-Ki67, 1:100 (BD Biosciences, cat. no. 550609); rabbit anti-lysozyme, 1:2,000 (Dako, cat. no. A0099); rabbit anti-ZO-1, 1:200 (Thermo Fisher Scientific, cat. no. 40-2200) and mouse anti-GFP, 1:400 (Abcam, cat. no. ab1218).

The secondary antibodies used were: goat anti-mouse Alexa Fluor 488 (Thermo Fisher Scientific, cat. no. A-11029); donkey anti-rabbit Alexa Fluor 488 (Thermo Fisher Scientific, cat. no. A-21206), goat anti-rabbit Alexa Fluor 555 (Thermo Fisher Scientific, cat. no. A-21429) and goat anti-mouse Alexa Fluor 405 (Abcam, cat. no. ab175660). All of the secondary antibodies were used at a dilution of 1:400. To label F-actin, phalloidin Atto 488 (Sigma-Aldrich cat. no. 49409) was used at 1:500 and phalloidin Alexa Fluor-647 (Thermo Fisher Scientific, cat. no. A22287) at 1:400.

For the immunostaining of tissue slices, rat anti-E-cadherin (ECCD-2; Thermo Fisher Scientific, cat. no. 13-1900) was used at 1:100, DAPI (Sigma-Aldrich, cat. no. D9542) was used at 5 µg ml$^{-1}$ and rhodamine–phalloidin (Thermo Fisher Scientific, cat. no. R415) was used at 1:200.

**Image acquisition.** All images, except those of laser cuts and in vivo immunostainings, were acquired using a Nikon TiE inverted microscope with a spinning disk confocal unit (CSU-WD, Yokogawa) and a Zyla sCMOS camera (Andor). For Supplementary Video 4, a ×40 objective (plan fluor; numerical aperture (NA), 0.75; dry) was used. For Fig. 6a, (first row of images) a 2×2 stitching grid was acquired with a ×20 objective (plan apo; NA, 075; Ph2; dry). For the remaining images, a ×60 objective (plan apo; NA, 1.2; water immersion) was used. For the live imaging experiments, a temperature box maintaining 37 °C in the microscope (Life Imaging Services) and a chamber maintaining $CO_2$ and humidity (Life Imaging services) were used. The open source Micromanager[57] was used to carry out multidimensional acquisitions with a custom-made script.

To image the monolayers on the 0.7 kPa gels (Figs. 3 and 4), the gels were mounted upside down to improve the image quality. Briefly, the samples were fixed in 4% PFA for 10 min at RT. They were then mounted in PBS and sealed with nail polish before being flipped and imaged from the apical side.

For laser ablation, images were acquired using a laser-scanning confocal microscope (LSM880, Carl Zeiss) at a resolution of 512×512 pixels (pixel size = 0.2595 µm) with a bidirectional scan. A Plan-Apochromat ×40 objective (NA, 1.3; oil; DIC M27) was used. The microscope was equipped with temperature control (37 °C), and $CO_2$ and humidity control. The Zeiss ZEN software was used to carry out the acquisitions.

For immunostainings of tissue slices, images were acquired using a laser-scanning confocal microscope (LSM880, Carl Zeiss) at a resolution of 1,024×1,024 pixels (pixel size = 0.2076 µm) with a bidirectional scan and a Plan-Apochromat ×40 objective (NA, 1.3; oil; DIC M27) in Airyscan mode. Imaging and Airyscan processing were performed using the Zeiss ZEN software.

**Three-dimensional traction microscopy.** The 3D tractions were computed as previously described[18]. Briefly, confocal stacks of the top layer of the fluorescent beads embedded in the PAA gels were imaged with a *z*-step of 0.2 µm both in the deformed (by the cells) and relaxed (trypsinized) states. From the stacks, the 3D deformations of the gel were computed with a homemade iterative 3D PIV software[18]. A window size of 64×64 pixels and an overlap of 0.75 was used. A Finite Element Method solution was implemented in ABAQUS to compute the 3D tractions from the 3D substrate displacements[18].

**Cell velocities.** To characterize the cell kinematics in Fig. 8, the velocity of the monolayer was computed by performing 3D PIV analysis on consecutive time-lapse images of organoid monolayers expressing membrane-targeted tdTomato (custom-made software; window size, 64×64 pixels; overlap, 0.75).

**Radial averaging and kymographs.** The boundary between the stem cell compartment and the transit amplifying zone was drawn by connecting the points where the normal traction component changed sign from negative to positive. If tractions were not available (as in immunostainings), the boundary was defined by the change in cell morphology (from columnar to elongated). For averaging (traction, velocity or image intensity), every pixel in the image was

assigned the value of the distance to the closest point of the contour of the stem cell compartment. Spatio–temporal diagrams (kymographs) of a given variable were obtained by binning the values of that variable as a function of the (signed) distance from the boundary of the stem cell compartment and then computing the mean for each bin. For vectors, the normal to the contour was determined by fitting a parametric parabola to the nine pixels surrounding each pixel of the contour. To attribute a normal vector to each pixel of the image, we followed the approach of Trepat and colleagues[45]. Briefly, for each pixel of the image, we first assigned the normal vector of the closest pixel of the contour of the stem cell compartment. We then smoothed the curvature and normal vector components using a moving average filter whose characteristic length increased with the distance from the contour. To build spatio–temporal kymographs, the process of masking and radial averaging was repeated for every time point. Additional crypts in the field of view were excluded from the analysis.

In Fig. 4c, the normal traction of the stem cell compartment was computed as the mean of the normal traction at the crypt centre. The normal traction of the transit amplifying zone was computed as the peak in positive normal traction within the first 20 µm outside the stem cell compartment.

**Averaging of crypt radial profiles.** Crypts are variable in size within a certain range. As a consequence, directly averaging profiles of tractions, velocity or any other parameter of the study generates artefacts arising from the misalignment of compartments between different crypts. To avoid this, individual crypt profiles were linearly resized to the average crypt radius of the experimental group. The resized profiles were then averaged.

**Blebbistatin treatment.** Organoid monolayers on 5 kPa gels (Fig. 4a–c) were imaged for 90 min in normal ENR medium (baseline). ENR medium containing blebbistatin (−/−; Sigma-Aldrich) was then added to a final concentration of 15 µM and the monolayers were imaged for 3 h. The medium was then aspirated, the sample was washed with ENR, and the monolayers were imaged for additional 11 h in normal ENR.

For the blebbistatin dosage experiments (Extended Data Fig. 3a–c), organoid monolayers on 5 kPa gels were treated with DMSO or blebbistatin (0.5, 1.5, 5 or 15 µM) in ENR medium. The monolayers were imaged 3 h after the treatment.

Monolayers on 0.7 kPa (Figs. 4d,e and 5b) or 15 kPa (Extended Data Fig. 5) gels were treated with 15 µM blebbistatin or DMSO (Sigma-Aldrich) in ENR medium for 3 h. They were then fixed in 4% PFA for 10 min at RT. Finally, they were washed twice with PBS and imaged as indicated earlier. The monolayers of Extended Data Fig. 5 were imaged without fixation. Crypt indentation (Fig. 4d) was quantified in Fiji by tracing a vertical line from the bottom of the crypt to the bottom of the cells of the transit amplifying zone in a lateral view of the monolayer.

**F-actin and myosin quantification.** Given the heterogeneity in the height of the different compartments of the organoid monolayer, we developed the following algorithm to define the cell apical, medial and basal coordinates for every $x$–$y$ position of the substrate. For the F-actin staining (phalloidin), each plane of the imaged $z$-stack was first binned (8 × 8 pixels). For each $x$–$y$ position of the binned image along the substrate, the apical and basal coordinates were then defined as the coordinates of the apical-most and basal-most peaks in fluorescence intensity (phalloidin). The medial position was defined as the $z$ coordinate equidistant to the apical and basal coordinate for each $x$–$y$ pixel. We then extracted the fluorescence intensity of the apical, medial and basal positions. A similar approach was used to quantify myosin IIA, but the Volume Manager plugin (by R. Haase, MPI-CBG) was used to segment the monolayer. This last approach was also used for F-actin quantification on 0.7 kPa PAA gels (Extended Data Fig. 3e), as the high indentation of the crypts on these soft substrates prevented accurate automatic segmentation of the apical and basal surfaces.

To quantify the myosin intensity of the crypt and villus in the tissue immunostainings, small rectangular regions of interest (ROIs) of about 10 pixels in width were manually drawn around the apical and basal surfaces on the F-actin channel. The myosin IIA intensity was then averaged in the longitudinal axis of each ROI to quantify the intensity of the peak. Two ROIs were quantified and averaged per position. To correct for changes in absolute intensity at different tissue depths, the values for each crypt–villus image were normalized by dividing all values by the apical intensity of the crypt bottom. Measurements were performed only in the crypt–villus regions that fitted in approximately three image planes (1 µm step) to avoid differences in intensity due to light penetration through the tissue.

**Quantification of cell tilt in vivo.** To quantify cell tilt in vivo, the cells were manually segmented in crypt images labelled with m-tdTomato or E-cadherin. An ellipse was fitted to each cell contour and cell orientation was defined as the angle of the ellipse long axis. The contour of the crypt was manually segmented and the normal direction to each pixel of the contour was calculated by fitting a parametric parabola to contour arcs of nine pixels (as described in the 'Radial averaging and kymographs' section). Cell tilt was defined as the angle difference between the normal to the crypt contour and the cell orientation. Tilt towards the crypt bottom was defined as positive. The tilt profiles obtained from each side of the crypt were averaged to generate one tilt profile per crypt. All crypt profiles were then rescaled to the average crypt contour length (in µm) and averaged.

**De novo crypt formation.** Organoids were cultured in ENR medium containing 10 µM CHIR99021 (SelleckChem) and 10 mM nicotinamide (Sigma-Aldrich). After 2 d, the organoids formed hyperproliferative spherical cysts devoid of crypts. For each PAA gel, we seeded the number of cysts contained in three Matrigel drops of a 24-well plate. The cysts were dissociated in TryplE (Gibco) at 37 °C for 5 min. Dissociation was mechanically assisted by pipetting and finally stopped by dilution in PBS supplemented with calcium and magnesium (Sigma-Aldrich). The cell suspension was then filtered through a cell strainer (40 µm diameter) to remove clumps of undissociated cells and centrifuged at 500$g$ for 5 min at RT. The pellet was resuspended in ENR containing 10 µM CHIR99021, 10 mM nicotinamide and 10 µM Y-27632 (Merck Millipore; ENR-CYN). The cells were seeded in a small volume (30 µl) on top of the micropatterned area of 5 kPa PAA gels. Functionalization and ECM micropatterning of the PAA gels was performed as described earlier using micropatterns of 600–900 µm in diameter. After incubation for 2 h at 37 °C and 5% $CO_2$, the unattached cells were washed out with 200 µl ENR-CYN, and 600 µl ENR-CYN was added. The medium was changed to ENR the following day. The ENR medium was refreshed on the third day after seeding.

Monolayers were fixed in 4% PFA at different timepoints (1, 2, 3 and 4 d after seeding) and immunostained for Olfm4, CK20 and F-actin (phalloidin) as described earlier. $Z$-stacks of the whole circular patterns were acquired with a ×20 objective by stitching four fields of view in a 2 × 2 grid, with a 20% overlap. A maximum intensity projection of each channel was generated for each field of view. The maximum intensity projections were then fused in Fiji with the plugin 'Grid/collection stitching'. Monolayers and Olfm4$^+$ foci were manually segmented, and their area and intensity were measured. The density of the Olfm4$^+$ foci was calculated as the ratio between the number of foci and the monolayer area. The CK20 intensity was measured in the segmented monolayer after excluding the Olfm4$^+$ foci. The background for each channel was estimated at regions outside of the monolayer and subtracted. All analyses were performed in Fiji.

The apical and basal F-actin intensities were automatically extracted from $z$-stacks acquired with a ×60 objective following the same approach explained above. The apical and basal F-actin intensities were then averaged over a circular ROI with a radius of approximately 16 µm located at the centre of the Olfm4$^+$ area or at a random position in the Olfm4$^-$ area.

For traction measurements, stacks of the cells and beads were acquired at the four indicated time points. The 3D tractions were measured as explained earlier. Tractions normal to the substrate were averaged over a circular region with a radius of approximately 16 µm at the centre of the developing crypts.

**Quantification of the area of the stem cell niche, and number of stem and Paneth cells.** Organoid monolayers seeded on PAA gels of varying stiffnesses were fixed and stained for F-actin (phalloidin) and Olfm4 as explained earlier.

The Olfm4$^+$ area was manually segmented. Cells in the Olfm4$^+$ area were manually counted in Fiji using the multipoint selection tool. Paneth cells were identified by their granular apical signal in bright-field and distinct apical actin signals. The number of stem cells was calculated by subtracting the number of Paneth cells from the total number of cells in the Olfm4$^+$ area.

**Laser cuts.** Laser ablation was performed using a Ti:Sapphire laser (Mai Tai DeepSee, Spectra Physics) set at 800 nm with a laser power of 15% (500–750 mW). Circular regions for ablation were manually selected at the boundary between crypt compartments based on basal cell morphology. The cuts were performed in the medial plane of the monolayer.

To compute the recoil velocities, PIV was performed using a window size of 16 × 16 pixels and an overlap of 0.75. The velocity fields were resized to the original image size (512 × 512) using a bicubic interpolation to compute velocities relative to the ablated region. A peak in tissue velocity occurred within the first 2 s after ablation and thus recoil velocity was computed in this time frame.

The contour of the ablated region was used to compute the radial and tangential components of the recoil velocity as explained earlier. The radial velocities were averaged according to their distances to the ablated region. Crypt indentation before and after ablation was computed from the deformation of fluorescent beads embedded in the substrate as explained in the 'Three-dimensional traction microscopy' section.

**Single-cell shape analysis.** *Image pre-processing.* Spinning-disc images of intestinal organoid monolayers were pre-processed to address low signal-to-noise ratios and image scattering at the apical and basal cell surfaces—presumably due to rich apical excretion, brush microvillar border and scattering in the hydrogel underlying the organoid monolayers. To enable automatic detection of all single-cell surfaces, the signal-intensity values in dim regions of the apical and basal surfaces were computationally increased. Using Fiji[58], the monolayer apical and basal surfaces were defined in 3D, following the contour of the monolayer by manually adding sparse points in the $x$–$z$ view and interpolating the surface between them, using the Volume Manager plugin (by R. Haase, MPI-CBG). Using a custom MATLAB script, image pixels lying on the capping surface with a fluorescence signal intensity

higher than the 1st and lower than the 3rd quartile of the overall image intensity were set to the value of the 3rd quartile (4th quartile in the case of extremely bright lateral cell surfaces), resulting in segmentable apical and basal membrane signals in cells that displayed only clear lateral surfaces in the original images.

*Cell segmentation.* Pre-processed cell-membrane images were used for automatic cell segmentation in MorphographX[59]. The images were processed with Gaussian blurring (sigma, 0.3–0.5) and stack normalization (radius, 4–10; blur factor, 0.5–0.8). Segmentation was performed in whole image stacks in 3D using the Insight Toolkit watershed algorithm implemented in MorphographX (threshold, 800–1,500). All segmentations required extensive manual correction for oversegmented, undersegmented and incomplete cells. Three-dimensional cell meshes were created (cube size, 2; smoothing, 1) from pixel label images for further shape analysis.

*Shape analysis.* Single-cell shape analysis was performed in 3D using custom-developed MATLAB tools. To account for the complex shape of the cells in the organoid monolayers, an apicobasal cell axis was constructed for each cell from the centroids of horizontal cell cross-sections in the central 70% of the cell body. The remaining 15% of the axis on each end was extrapolated as a straight line from the more stable central 70%. This 3D axis was used to calculate the 3D cell height and obtain new cross-sections normal to the cell axis. These cross-sections were analysed for their area and various shape parameters, resulting in detailed apicobasal shape profiles for all cells. Cell tilt to the crypt centre was defined as the angle of the straight end-to-end cell axis to the substrate normal (component in line with crypt centre), and set as <0 if the axis was pointing away from the crypt centre. Transit amplifying cells were defined as cells whose basal centroid lies within 14 µm of the manually outlined stem-cell niche border. Paneth cells were identified based on their distinct (granular) apical appearance in the corresponding bright-field images. All of the cells within the niche that were not Paneth cells were considered to be stem cells, in line with the Lgr5 and Olfm4 immunostaining results.

**Quantification of the cell division rate.** Maps of the spatial distribution divisions were manually obtained using Fiji multipoint selections. The coordinates of each cell division were imported to MATLAB. The mask of the stem cell compartment was used to compute the radial distance to the crypt centre of each pixel of the field of view as explained earlier. The radius of the stem cell compartment was divided into three equal regions and the rest of the monolayer was divided into circular regions of 8,1 µm (75 pixels). For each region, we divided the total number of divisions by the area of the region and the time of observation to calculate the cell division rate.

**Statistics and reproducibility.** Traction maps, kymographs and laser cuts were plotted in MATLAB. The remaining plots were generated in GraphPad Prism 8. Immunostain images and videos were processed with the open source software Fiji and HandBrake. The data are represented as the mean ± error (s.e.m. or s.d.; as indicated in the figure captions). Normality of the data was checked and the statistical test used to compare the means was chosen accordingly, as indicated in the figure captions. No statistical method was used to predetermine the sample size, a minimum of $n = 2$ experiments with multiple measurements per experiment were performed. No data were excluded from the analyses. The experiments were not randomized and the investigators were not blinded to allocation during the experiments or outcome assessment. When possible (cell traction and velocity, laser ablations and segmentation, among others), the experiments were automatically analysed using homemade software to avoid biases. All of the statistical analyses were performed in GraphPad Prism 8.

**Reporting Summary.** Further information on research design is available in the Nature Research Reporting Summary linked to this article.

## Data availability

The data that support the findings of this study are available from the corresponding authors on reasonable request. Source data are provided with this paper.

## Code availability

MATLAB analysis procedures and the code implementing the 3D vertex model calculations are available from the corresponding authors on reasonable request.

## References

54. Muzumdar, M. D., Tasic, B., Miyamichi, K., Li, L. & Luo, L. A global double-fluorescent Cre reporter mouse. *Genesis* **45**, 593–605 (2007).
55. Riedl, J. et al. Lifeact mice for studying F-actin dynamics. *Nat. Methods* **7**, 168–169 (2010).
56. Zhang, Y. et al. Mouse models of MYH9-related disease: mutations in nonmuscle myosin II-A. *Blood* **119**, 238–250 (2012).
57. Edelstein, A. D. et al. Advanced methods of microscope control using µManager software. *J. Biol. Methods* **1**, e10 (2014).
58. Schindelin, J. et al. Fiji: an open-source platform for biological-image analysis. *Nat. Methods* **9**, 676–682 (2012).
59. de Reuille, P. B. et al. MorphoGraphX: a platform for quantifying morphogenesis in 4D. *eLife* **4**, 05864 (2015).

## Acknowledgements

We thank J. Barbazán for assistance with laser ablations and discussions; E. Latorre for support with image segmentation and traction software; F. e. Marjou, M. A. Ziane, C. Cortina and X. Hernando for their support and training on organoid culture and in vivo procedures; and A. Marín, N. R. Chahare, T. Golde, J. Abenza, A. Ouzeri and all of the members of the Roca-Cusachs, Vignjevic, Arroyo and Trepat laboratories for their discussions and support. Funding: the authors are funded by the Spanish Ministry for Science, Innovation and Universities MICCINN/FEDER (grant nos PGC2018-099645-B-I00 to X.T. and PID2019-110949GB-I00 to M.A.), the Generalitat de Catalunya (Agaur; grant nos SGR-2017-01602 to X.T., 2017-SGR-1278 to M.A. and 2017-SGR-698 to E.B.; the CERCA Programme and 'ICREA Academia' award to M.A. and P.R.-C.), the European Research Council (grant nos Adv-883739 to X.T., CoG-681434 to M.A. and CoG-772487 to D.M.V.), the European Union's Horizon 2020 research and innovation programme grant agreement no. H2020-FETPROACT-01-2016-731957 and the Marie Skłodowska–Curie grant agreement nos 797621 to M.G.-G. and 792028 to F.G., 'La Caixa' Foundation (grant no. LCF/PR/HR20/52400004 to X.T. and P.R.-C., ID 100010434; fellowships LCF/BQ/DR19/11740013 to G.C., LCF/BQ/DE14/10320008 to C.P.-G. and 01/16/FLC to A.A.-V.), the Spanish Ministry of Health (grant no. SAF2017-86782-R to E.B.), Fundació la Marató de TV3 (project 201903-30-31-32 to X.T. and E.B.). IBEC, IRB and CIMNE are recipients of a Severo Ochoa Award of Excellence from the MINECO.

## Author contributions

C.P.-G. and G.C. performed all of the experiments, except for some of the immunostainings, which were performed by N.C., A.M. and V.R.G. C.P.-G., G.C., M.M. and M.G.-G. developed analysis software and analysed data. M.M. performed the image segmentation. D.K. and A.G.C. contributed in vivo myosin data. F.G., S.K. and M.A. implemented the computational model. A.A.-V., P.R.-C. and E.B. contributed technical expertise, materials and discussion. C.P.-G., D.M.V., M.A. and X.T. conceived the project. D.M.V., M.A. and X.T. supervised the project. C.P.-G., G.C., M.A. and X.T. wrote the manuscript.

## Competing interests

The authors declare no competing interests.

## Additional information

**Extended data** is available for this paper at https://doi.org/10.1038/s41556-021-00699-6.

**Supplementary information** The online version contains supplementary material available at https://doi.org/10.1038/s41556-021-00699-6.

**Correspondence and requests for materials** should be addressed to D.M.V., M.A. or X.T.

**Peer review information** *Nature Cell Biology* thanks Timothy Saunders, Benjamin Simons and Christian Dahmann for their contribution to the peer review of this work. Peer reviewer reports are available.

**Reprints and permissions information** is available at www.nature.com/reprints.

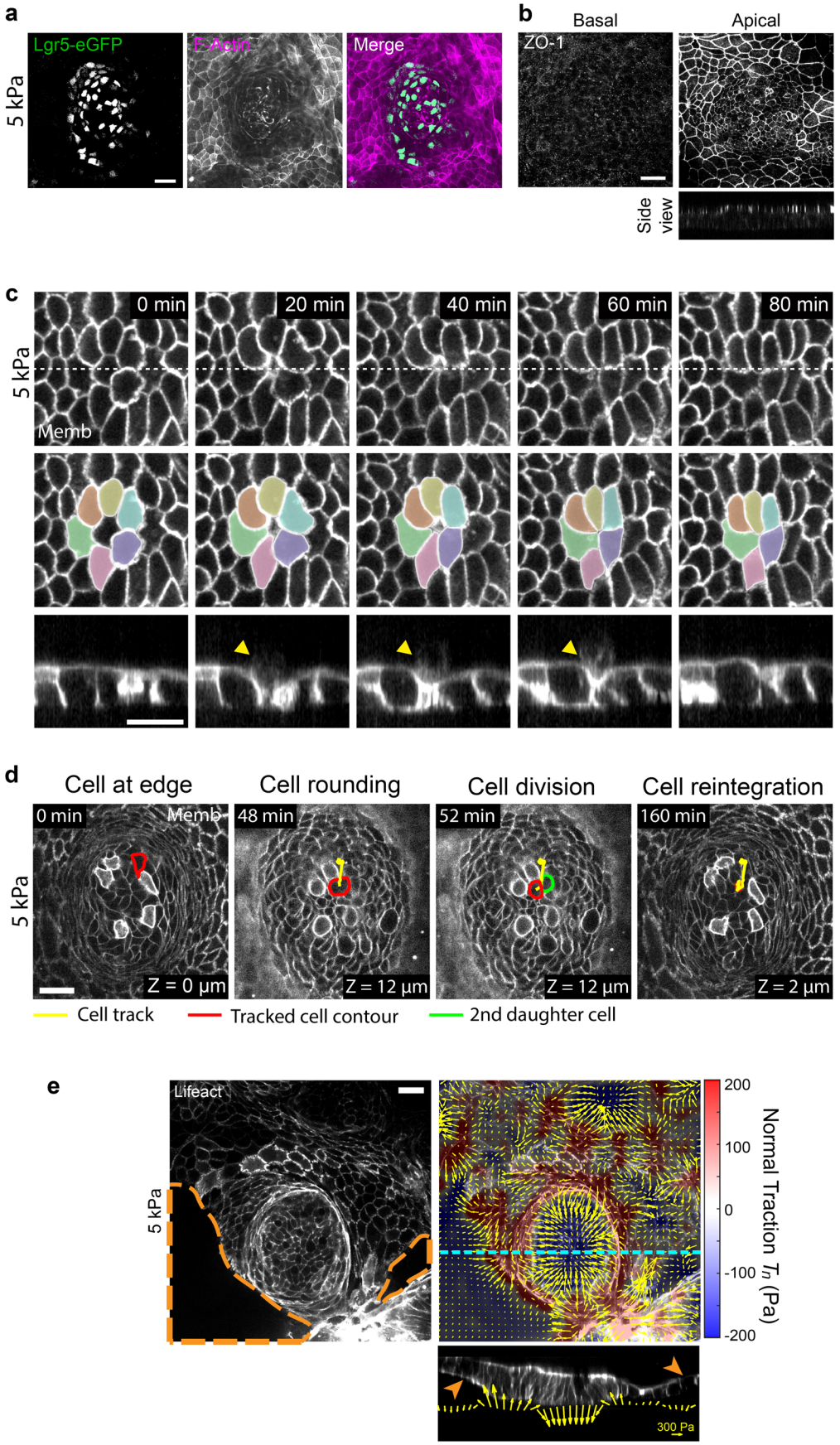


**Extended Data Fig. 1 | See next page for caption.**

**Extended Data Fig. 1 | Organoid monolayers capture key physiological features of the intestinal epithelium. a**, Organoid monolayers expressing Lgr5–eGFP-IRES-CreERT2 stained for GFP and F-actin (phalloidin). Representative image of 2 experiments. **b**, Organoid monolayers stained for Zonula occludens 1 (ZO-1). Top: Average intensity projections of the 10 most basal (Top left) or apical (Top right) planes of the monolayer. Bottom: lateral view of the monolayer. Representative image of 2 experiments. **c**, Snapshots of an extrusion event happening at the villus-like region. The extruding cell is indicated with the arrowhead in the orthogonal views (bottom row). The neighbours of the extruding cell are highlighted in colours in the top views of the monolayer (middle row). The lateral views correspond to the midplane indicated with a white dashed line at their corresponding top views (Top row). Representative of 9 extrusions from 3 experiments. **d**, Snapshots of a cell that exhibits retrograde flow due to division. The contour of the cell of interest is delineated in red. The track of this cell is delineated in yellow. The contour of the second daughter cell that appears after the division event is delineated in green. The first and last snapshots (0 min and 160 min) correspond to basal planes of the crypt (Z = 0 μm and 2 μm, respectively). Because division occurs apically, the second and third snapshots (48 min and 52 min), correspond to an apical plane where division is better observed (Z = 12 μm). 5 crypts from 3 experiments. **e**, Spontaneous formation of pressurized domes in the villus-like domain. Top left: medial view of an organoid monolayer expressing Lifeact–eGFP. The dashed orange line defines the regions where the monolayer has delaminated to form a pressurized dome (orange arrowheads in bottom panel). Top right: 3D traction map of the same crypt. Yellow vectors represent components tangential to the substrate and the colour map represents the component normal to the substrate. Horizontal cyan line indicates y-axis position of the lateral XZ view (bottom). Bottom: lateral view of the organoid monolayers. Yellow vectors represent tractions. Representative of 3 experiments. Scale vector, 300 Pa. All scale bars, 20 μm. Stiffness of all the gels, 5 kPa.

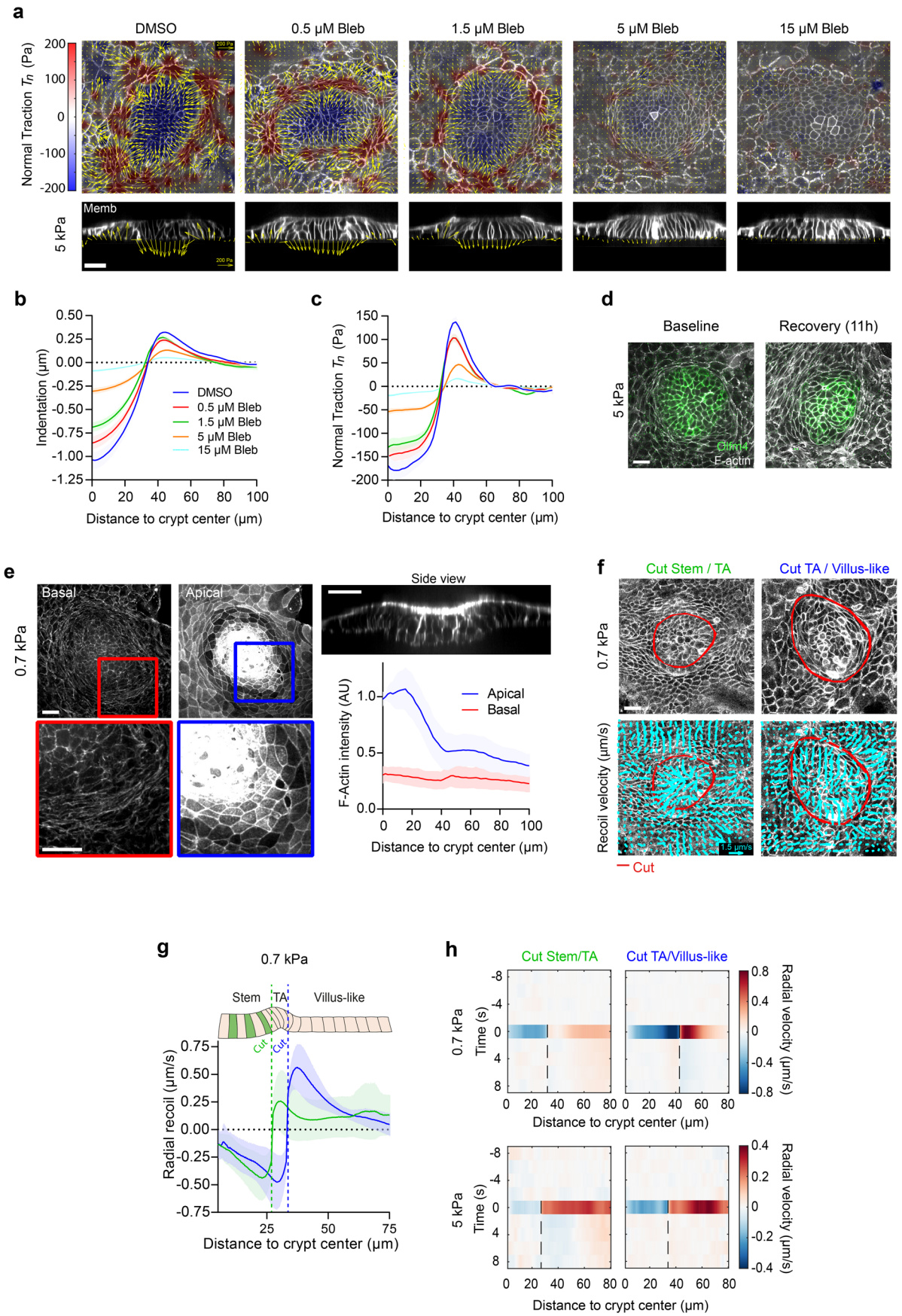


**Extended Data Fig. 2 | See next page for caption.**

**Extended Data Fig. 2 | Crypts fold through actomyosin-driven apical constriction. a**, Top row: 3D tractions of the crypts treated with the indicated concentration of blebbistatin (Bleb). Yellow vectors represent components tangential to the substrate and the colour map represents the component normal to the substrate. Bottom row: lateral views of the organoids along the crypt midline. Representative images from 3 independent experiments. Yellow vectors represent tractions. Scale bar, 20 μm. Scale vector, 200 Pa. **b-c**, Crypt indentation (**b**), and normal traction (**c**) as a function of the distance to the crypt centre for crypts treated with the indicated concentrations of blebbistatin for 3 h. Data are represented as mean ± s.e.m. of n = 18 (DMSO), 24 (0.5 μM), 19 (1.5 μM) 22 (5 μM) and 20 (15 μM) crypts from 3 independent experiments. **d**, Olfm4 immunostaining in membrane-tdTomato organoids at baseline conditions and 11 h after blebbistatin removal. Representative images from 2 independent experiments. Scale bar, 20 μm. **e**, Radial distribution of the apical (blue) and basal (red) F-actin intensity as a function of the distance to the crypt centre on 0.7 kPa substrates. Scale bars, 20 μm. Data are presented as mean ± s.d. of n = 12 crypts from 3 independent experiments. **f**, Bottom: Recoil velocity maps immediately after ablation of two crypts along the red lines on 0.7 kPa substrates. Left: a cut inside the TA. Right: a cut outside the TA. Scale vector, 1.5 μm/s. Top: the two crypts before ablation. Representative images from 3 independent experiments. Scale bar, 20 μm. **g**, Radial recoil velocity as a function of distance to crypt centre for cuts between stem cell compartment and transit amplifying zone (green) and between transit amplifying zone and villus-like domain (blue) on 0.7 kPa substrates. Data are represented as mean ± s.d. of n = 14 (cut Stem / TA) and 10 (cut TA / Villus-like) crypts from 3 independent experiments. **h**, Representative kymographs of circumferentially averaged radial velocity as a function of the distance to the crypt centre on 0.7 kPa (Top) and 5 kPa (bottom) substrates. Left: cut inside TA; right: Cut outside TA. The dashed black line indicates the time and position of the cut. Negative velocities point towards crypt centre.

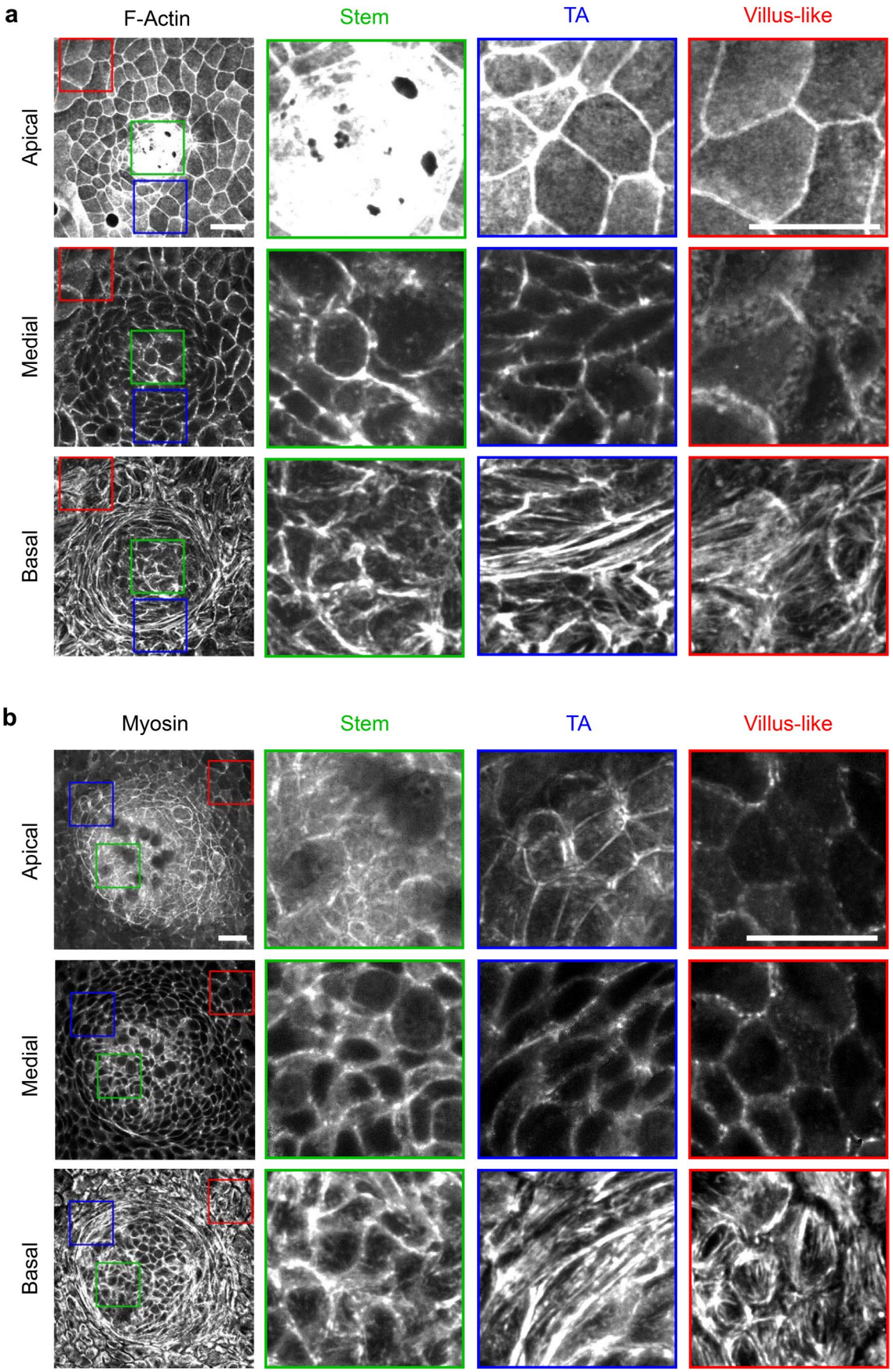


**Extended Data Fig. 3 | See next page for caption.**

**Extended Data Fig. 3 | Apicobasal distribution of F-actin and myosin in organoid monolayers. a-b**, Apical, medial and basal projections of F-Actin (Phalloidin, **a**) and myosin IIA-eGFP (**b**). The stem cell compartment (Stem), the Transit amplifying zone (TA) and the villus-like domain (villus-like) are zoomed in the regions of the monolayer indicated with the respective colours. Representative images from 4 (**a**) and 2 (**b**) independent experiments. Scale bars, 20 μm. Stiffness of the gel, 5 kPa.

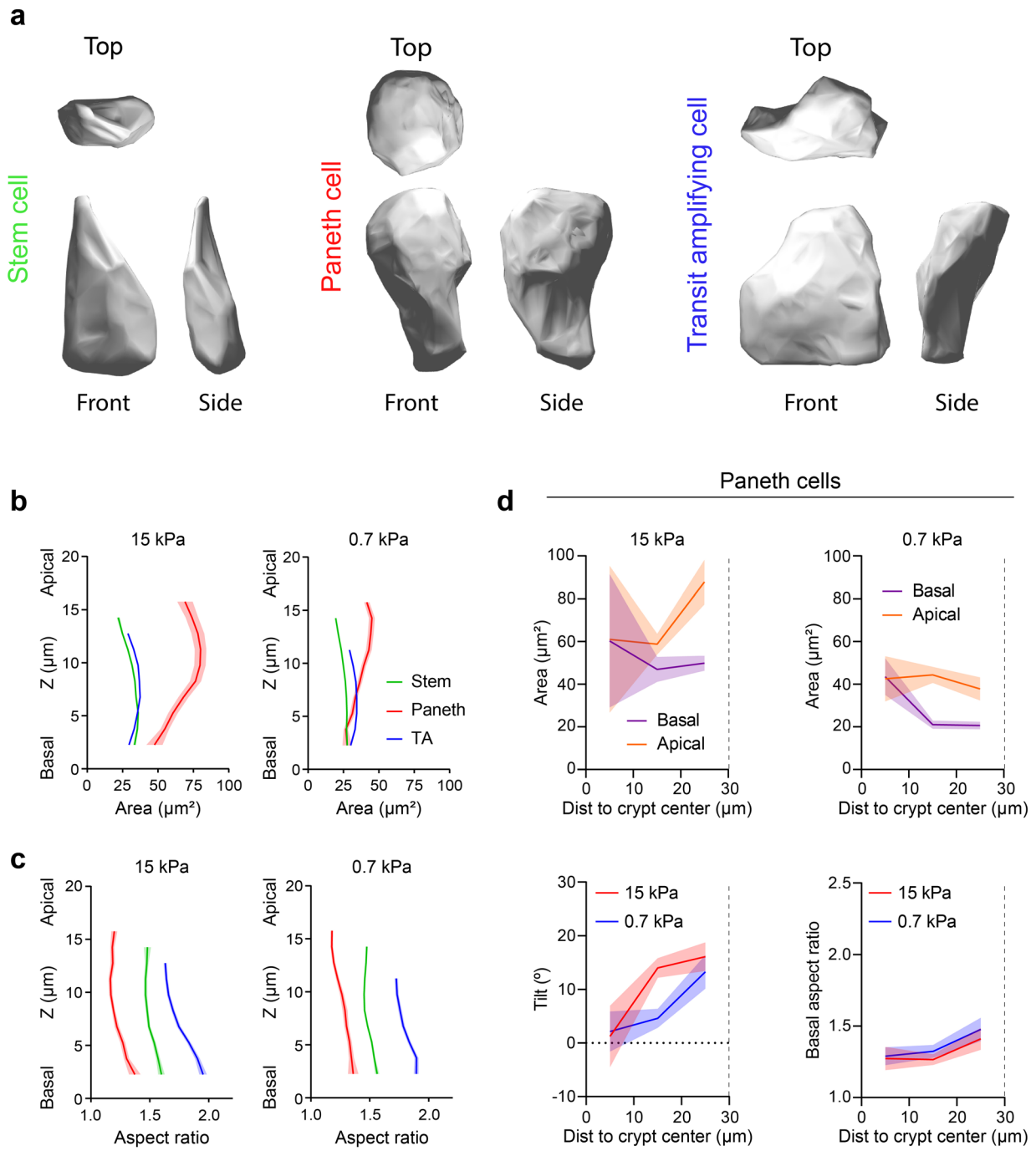


**Extended Data Fig. 4 | Morphometric analysis of the different cell types in the crypt. a**, Top, front and side 3D renders of a segmented stem cell (left), Paneth cell (centre) and transit amplifying cell (right). **b-c**, Cell area (**b**) and aspect ratio (**c**) along the apicobasal axis of stem (green), Paneth (red) and TA (blue) cells on rigid (left, 15 kPa) and soft (right, 0.7 kPa) gels. n = 190 (stem cells), n = 21 (Paneth cells); n = 218 (transit amplifying cells) for 15 kPa gels. n = 596 (stem cells); n = 52 (Paneth cells); n = 301 (transit amplifying cells) for 0.7 kPa gels. n = 3 crypts per stiffness from 2 (0.7 kPa) and 3 (15kPa) independent experiments. Data are represented as mean ± s.e.m. d, Top: Apical and basal area of Paneth cells as a function of the distance to the crypt centre on stiff (left, 15 kPa) and soft (right, 0.7 kPa) substrates. The boundary between the stem cell compartment and the transit amplifying zone is indicated in all the plots with a dashed vertical line. Bottom: Apicobasal tilt (left) and basal aspect ratio (right) of Paneth cells as a function of the distance to the crypt centre on stiff (red, 15 kPa) and soft (blue, 0.7 kPa) substrates. n = 3 crypts per stiffness from 2 (0.7 kPa) and 3 (15kPa) independent experiments. From centre to edge bins, n = 3, 7 and 10 cells for 15 kPa gels and n = 11, 25 and 15 cells for 0.7 kPa gels. Data are represented as mean ± s.e.m.

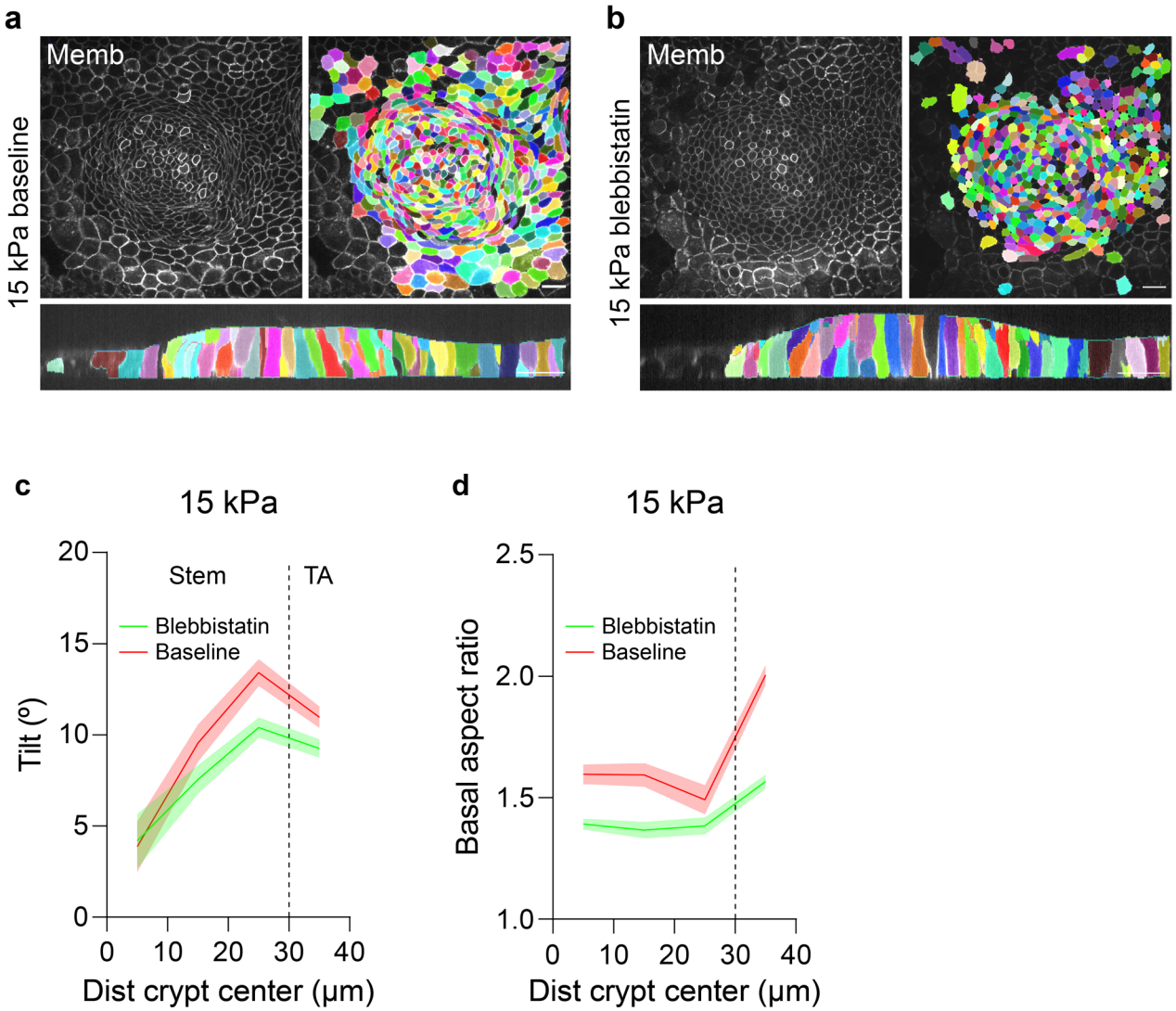


**Extended Data Fig. 5 | Effect of myosin inhibition on organoid cell shape. a-b**, 3D segmentation of a crypt on 15 kPa gels under baseline conditions (**a**) and the same crypt after 3 h treatment with 15 µM of blebbistatin (**b**). Top: medial view. Bottom: lateral view. Representative images of 2 independent experiments. Scale bar, 20 µm. **c-d**, Apicobasal tilt (**c**) and basal aspect ratio (**d**) as a function of the distance to crypt centre on rigid substrates (15 kPa) before and after blebbistatin. Vertical dashed line indicates the boundary between the stem cell compartment and the transit amplifying zone. From centre to edge bins, n = 42, 72, 150 and 232 cells for baseline crypt and 39, 82, 131 and 209 for blebbistatin treatment. Data from 2 independent experiments.

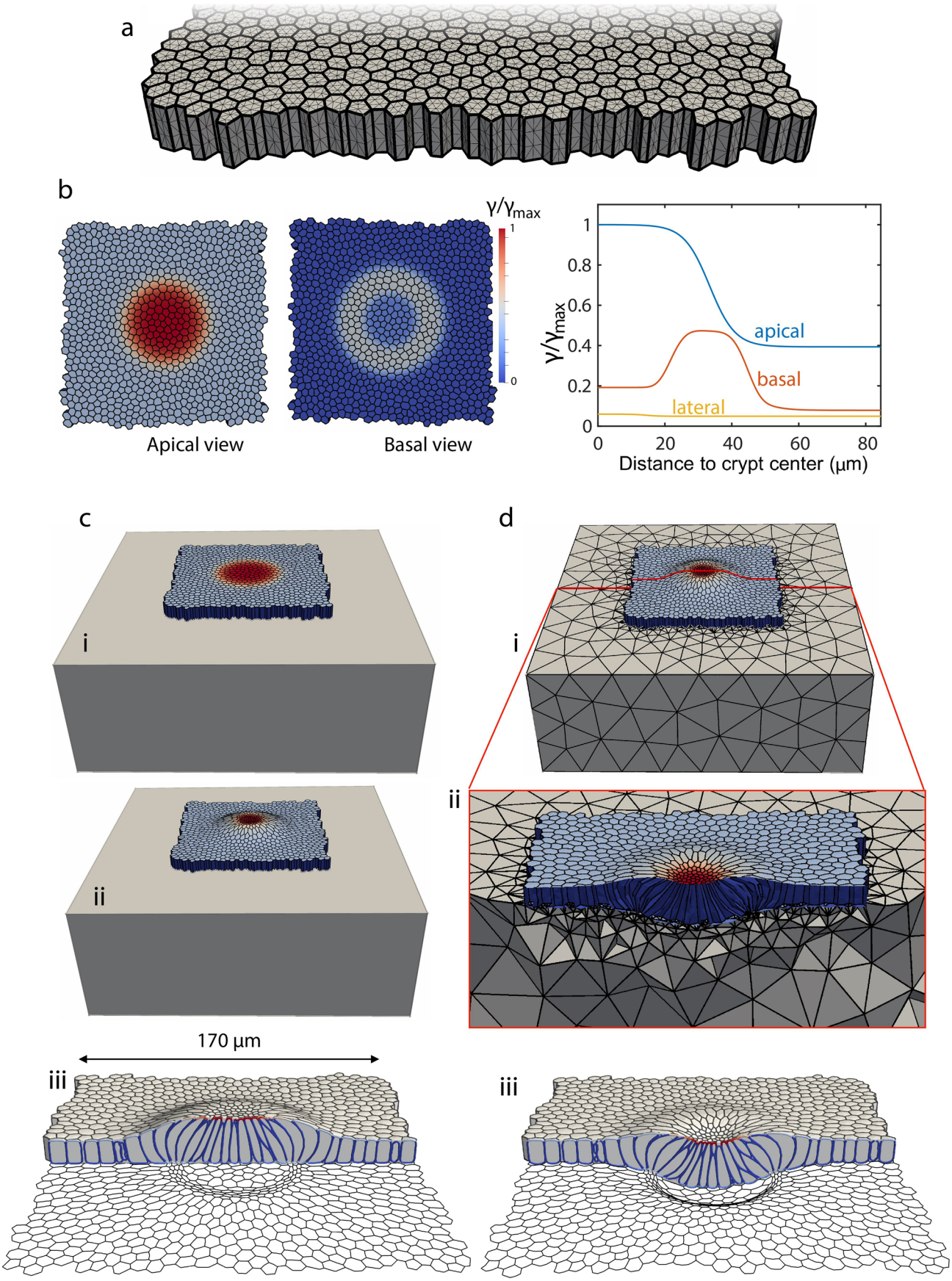


**Extended Data Fig. 6 | See next page for caption.**

**Extended Data Fig. 6 | 3D computational vertex model and simulation protocol. a**, Discretization of the tissue: the thick lines denote the intersection between cellular faces and the thin lines the triangulation of the cell surfaces. **b**, Pattern of apical, basal and lateral surface tensions prescribed in the initial regular cell monolayer. **c**, Equilibration of the initial regular monolayer with patterned surface tensions on a rigid substrate, where basal nodes are constrained to a plane but can slide horizontally. Initial state (i), equilibrated state (ii), and different view of equilibrated state with basal cell outline (iii). **d**, Coupling with a deformable substrate, modelled computationally with a tetrahedral mesh discretizing a hyperelastic block (i). The equilibrated crypt on a rigid substrate (**c**-ii) is further equilibrated on the deformable substrate (**d**-ii,iii).

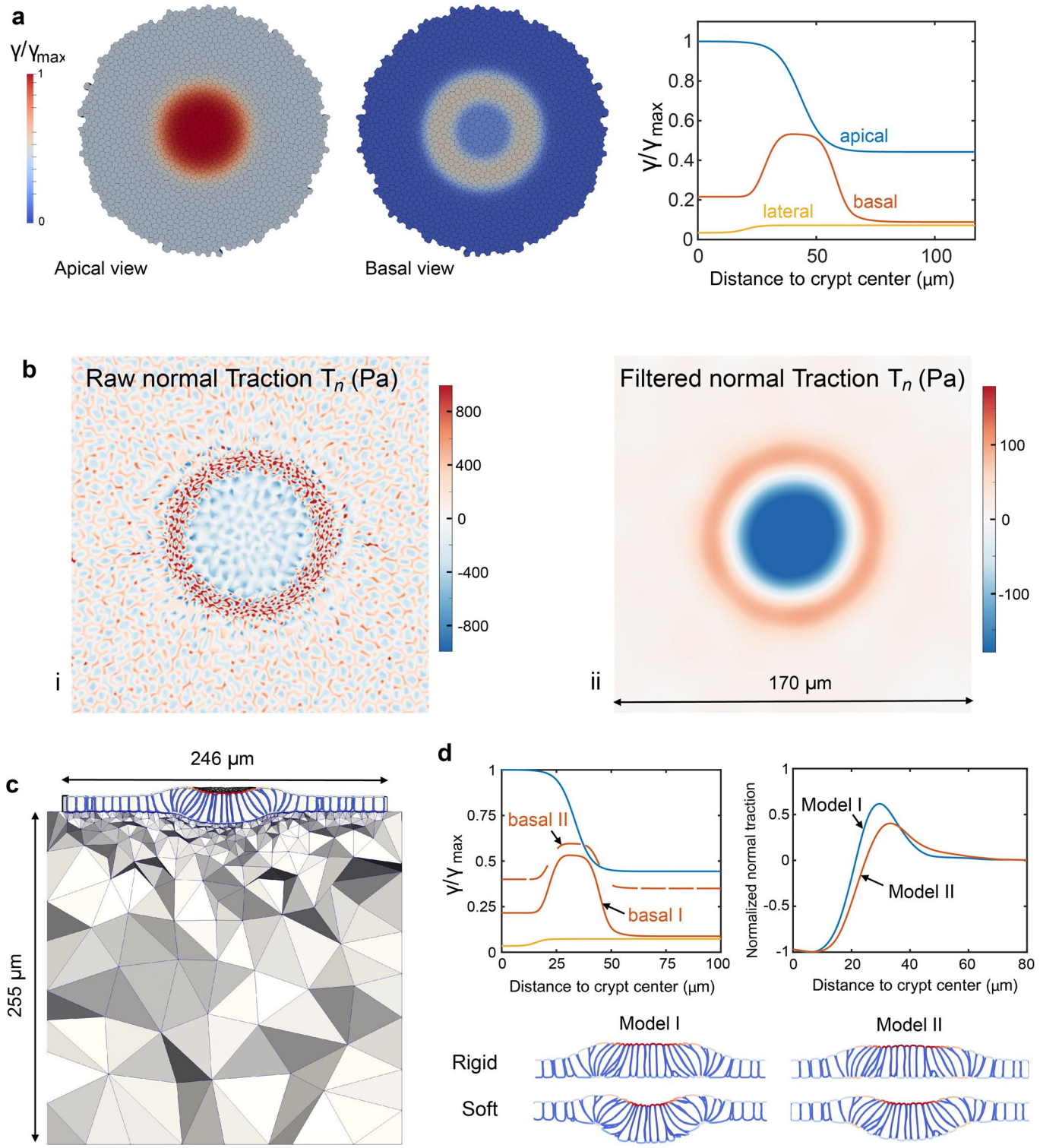


**Extended Data Fig. 7 | Simulation of crypt normal tractions. a**, Pattern of apical, basal and lateral surface tensions prescribed in the initial regular cell monolayer. **b**, Maps of basal normal traction. (i) Raw normal tractions at the basal plane featuring sub-cellular fine-scale details. To compare with experimental averages, we filtered these tractions with a Gaussian filter with standard deviation of 6 μm, (ii). **c**, Computational model of the deformed crypt on a soft hyperelastic substrate. **d**, Crypt folding for two models with different basal tension profiles on soft and rigid substrates.

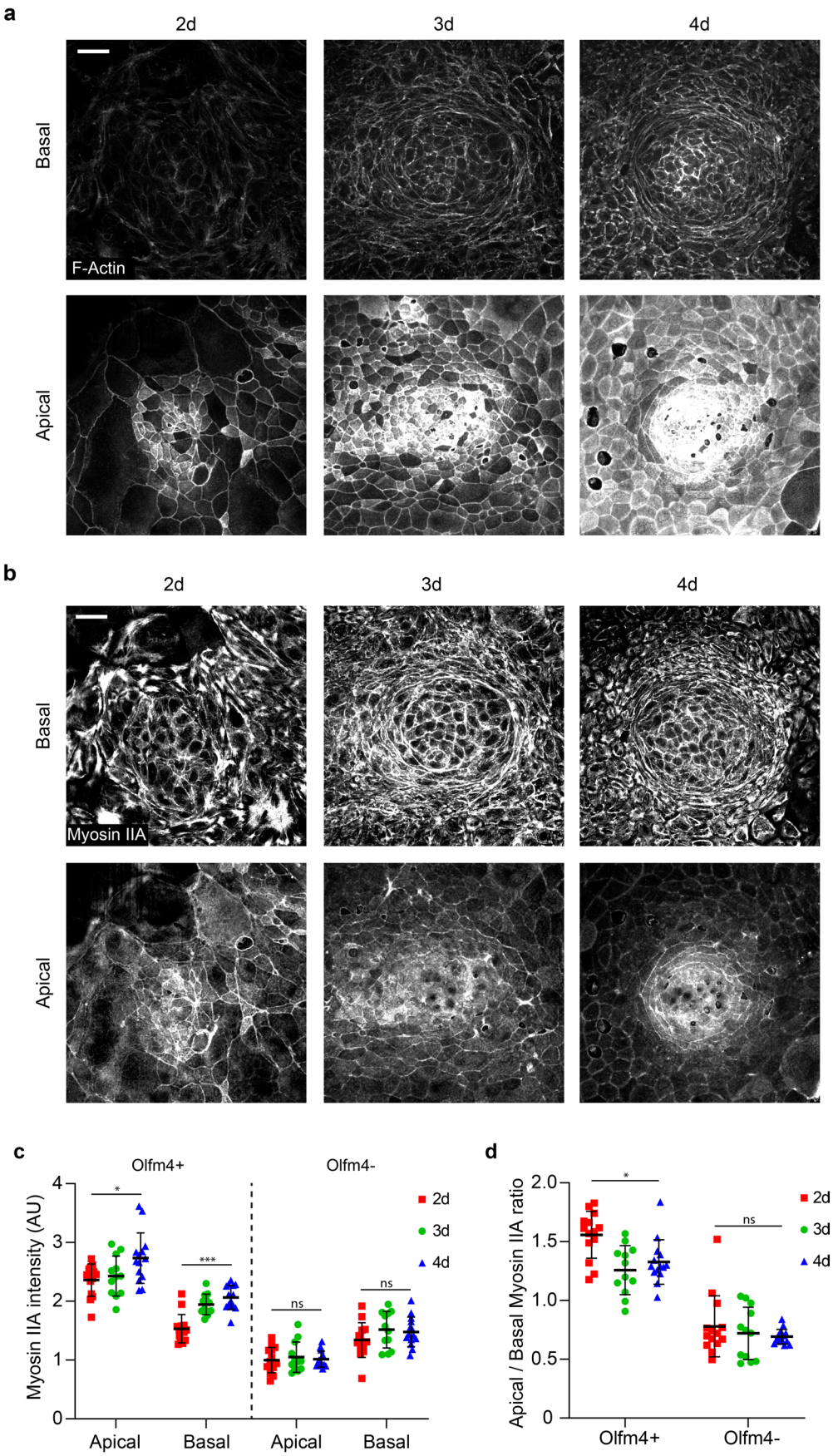


**Extended Data Fig. 8 | See next page for caption.**

**Extended Data Fig. 8 |** F-Actin and myosin IIA co-evolution during de novo crypt formation. **a-b**, Apical and basal projections of F-Actin (Phalloidin, **a**) and myosin IIA–eGFP (**b**) of crypts at the indicated timepoints (2 days, 3 days, 4 days). The crypts are the same as in Fig. 6a. Representative images of 2 independent experiments **c-d**, Quantification of apical and basal myosin IIA intensity (**c**) and apical/basal myosin IIA ratio (**d**) at the Olfm4 positive and Olfm4 negative regions for the indicated timepoints. n = 14 (2d), 12 (3d) and 14 (4d) crypts from 2 independent experiments. For all the graphs, data is represented as Mean ± s.d. All Scale bars, 20 μm. Stiffness of the gel, 5 kPa. * ($p < 0.05$) ***($p < 0.001$). Statistical significance was defined by a Kruskal–Wallis followed by a Dunn's multiple-comparison test (**c**: basal Olfm4+ and **d**) and one-way ANOVA followed by a Tukey multiple-comparison test (**c**: apical Olfm4 +, apical Olfm4- and basal Olfm4-). Only the statistical comparison between 2d and 4d is shown.

nature research

Corresponding author(s): Xavier Trepat, Marino Arroyo, Danijela Matic Vignjevic

Last updated by author(s): Apr 30, 2021

# Reporting Summary

Nature Research wishes to improve the reproducibility of the work that we publish. This form provides structure for consistency and transparency in reporting. For further information on Nature Research policies, see our Editorial Policies and the Editorial Policy Checklist.

## Statistics

For all statistical analyses, confirm that the following items are present in the figure legend, table legend, main text, or Methods section.

| n/a | Confirmed | |
|---|---|---|
| ☐ | ☒ | The exact sample size (*n*) for each experimental group/condition, given as a discrete number and unit of measurement |
| ☐ | ☒ | A statement on whether measurements were taken from distinct samples or whether the same sample was measured repeatedly |
| ☐ | ☒ | The statistical test(s) used AND whether they are one- or two-sided<br>*Only common tests should be described solely by name; describe more complex techniques in the Methods section.* |
| ☒ | ☐ | A description of all covariates tested |
| ☐ | ☒ | A description of any assumptions or corrections, such as tests of normality and adjustment for multiple comparisons |
| ☐ | ☒ | A full description of the statistical parameters including central tendency (e.g. means) or other basic estimates (e.g. regression coefficient) AND variation (e.g. standard deviation) or associated estimates of uncertainty (e.g. confidence intervals) |
| ☐ | ☒ | For null hypothesis testing, the test statistic (e.g. *F*, *t*, *r*) with confidence intervals, effect sizes, degrees of freedom and *P* value noted<br>*Give P values as exact values whenever suitable.* |
| ☒ | ☐ | For Bayesian analysis, information on the choice of priors and Markov chain Monte Carlo settings |
| ☒ | ☐ | For hierarchical and complex designs, identification of the appropriate level for tests and full reporting of outcomes |
| ☒ | ☐ | Estimates of effect sizes (e.g. Cohen's *d*, Pearson's *r*), indicating how they were calculated |

*Our web collection on statistics for biologists contains articles on many of the points above.*

## Software and code

Policy information about availability of computer code

| | |
|---|---|
| Data collection | Andor iQ3, MicroManager (version 1.4.22) and ZEN (ZEISS, version 2.3 SP1 FP3 black) were used for imaging |
| Data analysis | MATLAB. version 9.6.0.1072779 (R2019a), MathWorks Inc., Natick, Massachusetts, 2019 was used. Custom made codes can be made available upon request to the corresponding authors on reasonable request. MorphographX was used for 3D image segmentation. GraphPad Prism 8 was used for graph generation and for statistical analysis. ImageJ/Fiji was used to perform some image analysis and/or image pre-processing. ABAQUS version 6.14 (Dassault Systemes) software was used for Finite Element Method (FEM) calculations of traction forces. |

For manuscripts utilizing custom algorithms or software that are central to the research but not yet described in published literature, software must be made available to editors and reviewers. We strongly encourage code deposition in a community repository (e.g. GitHub). See the Nature Research guidelines for submitting code & software for further information.

## Data

Policy information about availability of data

All manuscripts must include a data availability statement. This statement should provide the following information, where applicable:

- Accession codes, unique identifiers, or web links for publicly available datasets
- A list of figures that have associated raw data
- A description of any restrictions on data availability

The data that support the findings of this study are available from the corresponding authors on reasonable request

# Field-specific reporting

Please select the one below that is the best fit for your research. If you are not sure, read the appropriate sections before making your selection.

☒ Life sciences ☐ Behavioural & social sciences ☐ Ecological, evolutionary & environmental sciences

For a reference copy of the document with all sections, see nature.com/documents/nr-reporting-summary-flat.pdf

# Life sciences study design

All studies must disclose on these points even when the disclosure is negative.

| | |
|---|---|
| Sample size | No statistical method was used to define sample size. A minimum of n=2 independent experiments were performed, with multiple measurements per experiment. Sample size was determined based on previous studies in the field (Serra-Picamal X. et al Nat Phys 2012, Bazellières E. et al. Nat Cell Bio 2015, Latorre E. et al. Nature 2018, Pérez-González C. et al. Nat Phys 2019). |
| Data exclusions | No data were excluded from the study. |
| Replication | Experiments were replicated at least twice. Replication of the data was at all times succesful. Experiments were performed at different days and with different organoid batches, obtaining the same results. |
| Randomization | For the experiments involving comparison between experimental groups, the samples were asigned randomly to each group. |
| Blinding | Researchers were not blinded to group allocation during data collection and/or analysis. Blinding was not possible as the same researcher both produced and analysed the data. |

# Reporting for specific materials, systems and methods

We require information from authors about some types of materials, experimental systems and methods used in many studies. Here, indicate whether each material, system or method listed is relevant to your study. If you are not sure if a list item applies to your research, read the appropriate section before selecting a response.

## Materials & experimental systems

| n/a | Involved in the study |
|---|---|
| ☐ | ☒ Antibodies |
| ☒ | ☐ Eukaryotic cell lines |
| ☒ | ☐ Palaeontology and archaeology |
| ☐ | ☒ Animals and other organisms |
| ☒ | ☐ Human research participants |
| ☒ | ☐ Clinical data |
| ☒ | ☐ Dual use research of concern |

## Methods

| n/a | Involved in the study |
|---|---|
| ☒ | ☐ ChIP-seq |
| ☒ | ☐ Flow cytometry |
| ☒ | ☐ MRI-based neuroimaging |

## Antibodies

| | |
|---|---|
| Antibodies used | The primary antibodies used and their respective dilutions were: rabbit anti Olfm4 1:200 (Cell Signaling Technology Cat# 39141, RRID:AB_2650511), mouse anti CK20 1:50 (Dako Cat# M7019, RRID:AB_2133718), mouse anti Ki67 1:100 (BD Biosciences Cat# 550609, RRID:AB_393778), rabbit anti Lysozyme 1:2000 (Dako Cat# A0099, RRID:AB_2341230), rabbit anti ZO-1 1:200 (Thermo Fisher Scientific Cat #40-2200, RRID:AB_2533456), mouse anti GFP 1:400 (Abcam Cat# ab1218, RRID:AB_298911) and rat anti-E-Cadherin 1:100 (ECCD-2; Thermo Fisher Scientific Cat# 13-1900, RRID:AB_2533005).<br><br>The secondary antibodies used were: goat anti mouse Alexa Fluor 488 (Thermo Fisher Scientific Cat# A-11029, RRID:AB_2534088), donkey anti rabbit Alexa Fluor 488 (Thermo Fisher Scientific Cat# A-21206, RRID:AB_2535792), goat anti rabbit Alexa Fluor 555 (Thermo Fisher Scientific Cat# A-21429, RRID:AB_2535850) and goat anti mouse Alexa Fluor 405 (Abcam Cat# ab175660, RRID:AB_2885184). All secondary antibodies were used at 1:400 dilution.<br><br>To label F-actin, Phalloidin Atto 488 (Sigma-Aldrich Cat# 49409) was used at 1:500; Phalloidin Alexa Fluor-647 (Thermo Fisher Scientific, Cat# A22287) was used at 1:400. For tissue slices, Rhodamine-phalloidin (Thermo Fisher Scientific Cat# R415) was used at 1:200. |
| Validation | All the antibodies were used for immunofluorescence. They were all validated by their respective manufacturers and by previous studies. Previous validations and citations can be found by using RRID numbers specified above. |

## Animals and other organisms

Policy information about studies involving animals; ARRIVE guidelines recommended for reporting animal research

| | |
|---|---|
| Laboratory animals | Organoids were cultured from 3-6 months old mice (mixed background) expressing membrane-targeted tdTomato, lifeact-eGFP, MyosinIIA-eGFP or Lgr5-eGFP-IRES-CreERT2. Organoids were obtained from male and female mice and no sex-specific differences were observed. |
| Wild animals | This study did not involve wild animals. |
| Field-collected samples | This study did not involve samples collected from the field. |
| Ethics oversight | Animal experimentation was approved by the Animal care and Use Committee of Barcelona Science Park (CEEA-PCB) and Animal Welfare Body, Research Centre, Institut Curie. All procedures were carried out in compliance with the European Regulation for the Protection of Vertebrate Animals used for Experimental and other Scientific Purposes (Directive 2010/63). |

Note that full information on the approval of the study protocol must also be provided in the manuscript.